

A COMPUTATIONAL STUDY OF SPIN-DEPENDENT CURRENT FLOW THROUGH QUANTUM WIRES

A Project Report

submitted by

ALFRED AJAY AUREATE R

*in partial fulfilment of the requirements
for the award of the degree of*

DUAL DEGREE

*under the guidance of
Dr. Anil Prabhakar*



**DEPARTMENT OF ELECTRICAL ENGINEERING
INDIAN INSTITUTE OF TECHNOLOGY, MADRAS.**

May 2015

THESIS CERTIFICATE

This is to certify that the thesis entitled **A computational study of spin-dependent current flow through quantum wires**, submitted by **Alfred Ajay Aureate R**, to the Indian Institute of Technology, Madras, for the award of the degree of **Dual Degree**, is a bona fide record of the research work carried out by him under my supervision. The contents of this thesis, in full or in parts, have not been submitted to any other Institute or University for the award of any degree or diploma.

Dr. Anil Prabhakar

Project Guide

Professor

Dept. of Electrical Engineering
IIT-Madras, Chennai - 600 036

Place: Chennai

Date: 6th May, 2015

ACKNOWLEDGEMENTS

I would like to take this opportunity to thank my family for their invaluable support and encouragement throughout my life, without which I wouldn't have been a part of such a prestigious institution. I would like to dedicate this work to them.

I'd sincerely like to thank my project guide, Prof. Anil Prabhakar, for always being there whenever I had difficulties even with his busy schedule and for supporting me to work on things that I loved. I'm very grateful for the time that he spent so patiently making me understand a lot of concepts, some of which were very rudimentary. Also I would like to thank him for streamlining my progress sometimes, towards the milestones that I wanted to achieve.

I'd like to thank others who were part of Magnonics & Spintronics group - Nikhil, Guru and Malathi madam for providing me guidance whenever I wanted to check the correctness of my ideas. The insights of the cutting edge research they provided me in those fields helped me a lot in understanding the state-of-the-art technologies. I'd like to thank my labmates too for providing me a congenial and an inquisitive working environment.

ABSTRACT

This report studies the behaviour of current flow across interfaces involving ferromagnetic materials. The spin-dependence of such a current flow shows various significant properties that are applied in a lot of recent devices, like Giant Magneto Resistance (GMR), Tunnel Magneto Resistance (TMR), Spin-Transfer Torque (STT), etc. Also, recently there is a huge demand for the reduction in size of all kinds of electronic devices including the memory-based systems. So, using quantum wire and quantum dot based devices seem to offer better alternatives.

We have concentrated on the behaviour of TMR and STT in magnetic tunnel junctions and metal-ferromagnet interfaces respectively for nanowires (or nanopillars) of various sizes. We have also compared those properties to junctions and interfaces that are spread few orders of magnitude wider than the de Broglie wavelength of the electrons or holes. Hence, we studied how lateral confinement changes the spin-dependent properties.

First, the electron wavefunction of the quantum wire was simulated using various methods by solving the time-independent Schrodinger's equation. Then, the allowed eigen energies obtained by solving that equation were used to study the behaviour of various wave vectors that were allowed to flow through the nanowires. This helped us in analysing the behaviour of several spin-dependent properties.

TABLE OF CONTENTS

ACKNOWLEDGEMENTS	i
ABSTRACT	ii
LIST OF TABLES	vi
LIST OF FIGURES	viii
1 Introduction	1
1.1 Semiconductor nanostructures	1
1.1.1 Importance and relevance	1
1.1.2 Classification	1
1.2 Quantum wires	2
1.2.1 Properties	2
1.2.2 Application	2
2 Simulating quantum wires	3
2.1 Quantum modelling	3
2.2 Simulation using variable separation method	4
2.2.1 Rectangular quantum wire	4
2.2.2 Circular quantum wire	7
2.3 Simulation using finite difference method	11
2.3.1 Rectangular quantum wire	11
2.3.2 Circular quantum wire	14
2.4 Simulation of quantum dot using mesh-based methods	17
2.5 Simulation using LOBPCG method	18
2.5.1 Eigen energy levels of a rectangular quantum wire	18
2.5.2 Eigen energies for wires of different dimensions	20
2.5.3 Eigen energy levels of an array of 4 quantum wires	20
2.5.4 Variation of eigen energies due to outside potential	21

2.5.5	Eigen energy levels as the gap between the 4 wires is varied	23
3	Tunneling Magneto Resistance	25
3.1	Theory and importance of TMR	25
3.1.1	Spin of an electron	25
3.1.2	TMR of magnetic tunnel junctions	25
3.1.3	Theories explaining TMR	26
3.1.4	Free electron model	26
3.2	Variation of transmission probability with the thickness d of the insulating barrier . . .	30
3.2.1	Parallel alignment	31
3.2.2	Anti-parallel alignment	31
3.3	Variation of tunneling conductance with the thickness d of the insulating barrier . . .	32
3.3.1	Planar magnetic tunnel junction	33
3.3.2	Nanowire magnetic tunnel junction	33
3.4	Variation of TMR with the thickness d of the insulating barrier	33
3.5	Behaviour of transmission probability with the barrier potential V_B	35
3.5.1	Parallel alignment	35
3.5.2	Anti-parallel alignment	36
3.6	Behaviour of tunneling conductance with the barrier potential V_B	36
3.6.1	Planar magnetic tunnel junction	38
3.6.2	Nanowire magnetic tunnel junction	38
3.7	Behaviour of TMR with the barrier potential V_B	38
3.8	Tunneling parameters for an array of 4 quantum wires	39
3.8.1	Tunneling conductance vs gap between wires	39
3.8.2	Tunneling Magneto Resistance (TMR) vs gap between wires	40
4	Spin Transfer Torque	41
4.1	Theory and applications of Spin Transfer Torque	41
4.1.1	Metal-Ferromagnetic junction	41
4.1.2	Particle Transport	41
4.1.3	Spin Transport	42
4.2	Free Electrons	43
4.2.1	Spin filtering	45

4.2.2	Spin Rotation	45
4.2.3	Spatial precession	48
4.3	Distribution of electrons	48
4.3.1	Transverse spin current for different wire sizes	50
4.3.2	Spin Transfer Torque for different wire sizes	52
5	Conclusion and future scope for work	54
	REFERENCES	55

LIST OF TABLES

2.1 Errors in the simulation	11
--	----

LIST OF FIGURES

1.1 Quantum wells, wires and dots	2
2.1 ψ for rectangular quantum wire at different energy levels	5
2.2 Relative error in ψ for rectangular quantum wire at different energy levels	6
2.3 Error percentage variation	7
2.4 ψ for circular quantum wire when $m = 1$	9
2.5 ψ for circular quantum wire with $m = 3$	10
2.6 Error in ψ for circular quantum wire with $m = 1$	10
2.7 Error in ψ for circular quantum wire with $m = 3$	11
2.8 Normalized ψ for rectangular quantum wire at different energy levels	12
2.9 Error in ψ for rectangular quantum wire at different energy levels	13
2.10 Maximum and mean error in ψ for different no. of iterations, for rectangular quantum wire when $n_x = 1, n_y = 2$	14
2.11 Normalized ψ for circular quantum wire at different energy levels	15
2.12 Error in ψ for circular quantum wire at different energy levels	16
2.13 Maximum and mean error in normalized ψ for circular quantum wire at $n_\rho = 1, n_\phi = 1$	17
2.14 Normalized ψ for quantum dots - ground state	17
2.15 First 9 eigen energy levels of a square quantum wire	19
2.16 Eigen energies (in eV) of a square quantum wire for first 9 energy levels	19
2.17 E_{2D} (in eV) vs l_w ($\times 10^{-10}$ m)	20
2.18 First 9 eigen energy levels of 4 quantum wires	21
2.19 Eigen energies (in eV) of a square quantum wire for first 9 energy levels	21
2.20 Ground state energy for different $V_{outside}$ (in eV)	22
2.21 E_{2D} (in eV) vs $V_{outside}$ (in eV) for first 9 eigen energy levels	22
2.22 Ground state energy for different gaps (in nm) between the wires	23
2.23 E_{2D} (in eV) vs gap between the wires (in nm) for first 9 eigen energy levels	24
3.1 (a) Potential energy diagram for a metal/insulator/metal tunnel junction with the bias voltage V (b) The geometry of one- electron potential	27

3.2	Densities of states for spin-up ($D \uparrow$) and spin-down ($D \downarrow$) electrons in the F alignment (a) and those in the A alignment (b) ^[17]	29
3.3	Geometries of the potentials for spin-up and spin-down electrons in the F alignment are shown in panels a) and (b), and those in the A alignment are shown in (c) and (d), respectively	30
3.4	Transmission probability, T_F vs barrier length d for nanowire ($V_B = 2.2V$)	31
3.5	Transmission probability, T_A vs barrier length d ($V_B = 2.2V$)	32
3.6	Tunneling conductance per unit area vs barrier length d ($V_B = 2.2V$)	32
3.7	Relative tunneling conductance vs barrier thickness ($V_B = 2.2V$)	33
3.8	TMR vs barrier thickness, d for different wire dimensions $V_B = 2.2V$	34
3.9	Transmission probability, T_F vs barrier potential V_B ($d = 10nm$)	35
3.10	Transmission probability, T_A vs barrier height V_B ($d = 10nm$)	36
3.11	Tunneling conductance per unit area vs barrier potential V_B ($d = 10nm$)	37
3.12	Relative tunneling conductance vs barrier potential V_B ($d = 10nm$)	37
3.13	TMR vs barrier height V_B for different wire dimensions ($d = 10nm$)	38
3.14	Tunneling conductances vs gap between wires	39
3.15	TMR vs gap between wires	40
4.1	Spin filtering of spin currents for a free electron	46
4.2	Spin rotation of spin currents for a free electron	47
4.3	Spatial spin precession of spin currents for a free electron	47
4.4	Incident and reflected transverse spin current density vs l_w in nm	51
4.5	$Q_{transmitted}^{(transverse)}$ vs K_Fx for different wires	51
4.6	Spin Transfer Torque vs K_Fx for different wires	52
4.7	Spin Transfer Torque vs l_w at $K_Fx = 10$	53

CHAPTER 1

Introduction

1.1 Semiconductor nanostructures

1.1.1 Importance and relevance

When one or more of the dimensions of a solid are reduced sufficiently, its physicochemical characteristics significantly change from those of the bulk solid. With reduction in size, novel electrical, mechanical, chemical, magnetic, and optical properties can be introduced, which is what is actually used in a lot of devices nowadays. The resulting structure is then called a low-dimensional structure (or system). The confinement of electrons and holes to these low-dimensional structures changes a lot of properties. The size effects are so much that quantum effects need to be taken into account.

Some of the physicochemical properties shown by the low-dimensional materials are not shown by the corresponding large-scale structures of the same composition. Nanostructures are low-dimensional structures with one or more of their dimensions falling into nanometer regime or molecular scales. These nanostructures constitute a bridge between molecules and bulk materials. Suitable control of the properties and responses of nanostructures can lead to new devices and technologies.

Ever since the discovery/invention by Esaki and Tsu in the 1970s, semiconductor quantum wells and superlattices have evolved from scientific curiosities to a means of probing the fundamentals of quantum mechanics, and more recently into wealth-creating semiconductor devices^[1].

1.1.2 Classification

Classifying different low-dimensional structures based on the number of dimensions confined (fig 1.1):

Three-dimensional (3D) structure or bulk structure: No quantization of the particle motion occurs, i.e., the particle is free. It's like just considering a bulk of semiconductor.

Two-dimensional (2D) structure or quantum well: A quantum well is a potential well with allowing only discrete energy values. It confines electrons or holes in one dimension and allows free propagation in two dimensions. Quantum wells are formed in semiconductors by having a material like gallium arsenide sandwiched between two layers of a material with a wider bandgap, like aluminium arsenide.

One-dimensional (1D) structure or quantum wire: In condensed matter physics, a quantum wire is an electrically conducting wire in which quantum effects influence the transport properties. It confines electrons or holes in two spatial dimensions and allow free propagation in the third. The carbon nanotube is an example of a quantum wire.

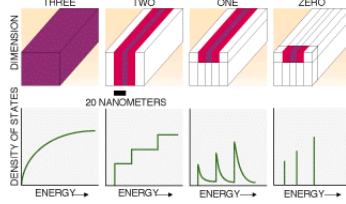


Figure 1.1: Quantum wells, wires and dots

Zero-dimensional ($0D$) structure or quantum dot: A quantum dot is a nanocrystal made of semiconductor materials that are confined in a space small enough to exhibit quantum mechanical properties. Specifically, its excitons are confined in all three spatial dimensions. The electronic properties of these materials are intermediate between those of bulk semiconductors and of discrete molecules.

In this report, we are interested only in modelling the properties influenced by the quantum wire structures alone. Especially the conducting properties in the presence of electric field with some modifications in the geometry. Influence of magnetic field is not considered here.

1.2 Quantum wires

1.2.1 Properties

A conductor will show ohmic behavior as long as its dimensions are much larger than (1) the electron de Broglie wavelength, (2) the mean free path, and (3) the phase-relaxation length^[2].

Quantum wires are mesoscopic devices which are good conductors in one direction but quantized in the orthogonal directions, which leads to quantized values of the conductance. It follows from very general arguments (see [2]) that the conductance per transverse mode per electron is equal to $\frac{e^2}{h}$. Hence, the conductance of a quantum wire is $\frac{2e^2 M}{h}$ where M is the number of modes in the energy range $\mu_1 < E < \mu_2$ and μ_1 and μ_2 are the chemical potentials on either side of the conductor. The factor of 2 accounts for the two possible spins of the electron.

1.2.2 Application

1. Optoelectronics, microelectronics, field emission devices, photonics, clothing fabric, and electronic device applications
2. As photon waveguides, when two quantum wires cross each other the juncture acts as a quantum dot. It is therefore possible that semiconductor quantum wire crossings will be important to the future of digital computing.
3. Because of their high aspect ratio, nanowires are also uniquely suited to dielectrophoretic manipulation^{[3],[4]}, which offers a low-cost, bottom-up approach to integrating suspended dielectric metal oxide nanowires in electronic devices such as UV, water vapor, and ethanol sensors^[5]. Though there are other uses for quantum wires beyond these, the only ones that actually take advantage of physics in the nanometer regime are electronic.

CHAPTER 2

Simulating quantum wires

2.1 Quantum modelling

About a century back, it was understood without any doubt that quantum mechanical picture was more accurate than the classical picture in describing the real life physical phenomena. But, the difference in accuracy is significant only when spatial dimensions considered are close to the nanometer regime and at molecular or atomic scales. For example, classical mechanics is enough to calculate the amount of fuel required to run a vehicle, the water flow rate in a pipe, current through a resistor, etc. Whereas, the properties of atom, chemical bonds, motion of an electron in a crystal, etc., can only be explained using quantum mechanical laws.

Moreover, many phenomena exhibited on a macroscopic scale reveal underlying quantum phenomena. It is in this reductionist sense that quantum mechanics is proclaimed as the basis of our present understanding of all natural phenomena studied and exploited in chemistry, biology, physics, materials science, engineering, etc. Physical behaviour at the nanoscale is accurately predicted by quantum mechanics, as represented by the Schrodinger's equation, which therefore provides a quantitative understanding of the properties of low-dimensional structures.

Need for quantum modelling at nanoscale

In quantum mechanics, the trajectory of a moving particle loses its meaning when the distance over which potential energy is varying is on the order of the de Broglie wavelength: $\lambda = \frac{2\pi}{\sqrt{2mE}}\hbar$ where \hbar is the reduced Planck constant, m is the mass of the particle, and E is its energy. In other words, a basic characteristic of all matter at the nanoscale is the manifestation of the wave-particle duality - a fundamental quantum-mechanical principle that states that all matter (electrons, nuclei, photons, etc.) behaves as both waves and particles. The quantum effects of confinement become significant when at least one of the dimensions of a structure is comparable in length to the de Broglie wavelength. If at least one dimension of a solid is comparable to the de Broglie wavelength of the particle, a quantum-mechanical treatment of particle motion becomes necessary.

Electron wavefunction and Schrodinger's equation

In the Schrodinger description of quantum mechanics, an elementary particle e.g., an electron, a hole and a photon or even a physical system such as an atom is described by a wave function $\psi(r, t)$, which depends on the variables describing the degrees of freedom of the particle (system). The square of the wave function is interpreted as the probability of finding a particle at spatial location $\vec{r} = (x, y, z)$ and time t . The wave function contains all of the information that may be obtained about a physical entity

and is sufficient to describe a particle or system of particles. In other words, if the wave function of, for example, an ensemble of electrons in a device, is known, it is possible in principle - though limited by computational abilities - to calculate all of the macroscopic parameters that define the electronic performance of that device^[6].

In this project, simulation of the quantum wire was done using Python (2.7.6) programming language, implementing various methods for numerically solving the following eigen value equation which is the time-independent Schrodinger's Equation (SE):

$$-\frac{\hbar^2}{2m^*} \nabla^2 \psi + V\psi = E\psi \quad (2.1)$$

where \hbar is reduced Planck's constant, m^* is the effective mass of an electron in crystal (here, this effective mass is approximated to be constant for all potentials), ∇ is the Poisson operator ($\nabla \equiv \sum_i \frac{\partial}{\partial x_i}$ where i represents the dimensions considered), E is the energy of an electron, V is the potential applied in the region of interest and ψ is the probability amplitude of the electron wavefunction. $|\psi|^2$ gives the probability of finding an electron at a point. For simplicity, initially only the case where zero potential ($V = 0$) inside the quantum wire region and infinite potential outside, is considered. The wavefunction is also initialized differently for different methods. Whereas, at the boundaries, it is always maintained zero (but only when infinite potential is considered outside). Also, in all the cases below, only the cross-section of the wavefunction ψ , perpendicular to the axis of the quantum wire is shown in the figures. First, square symmetric potential is considered, i.e., quantum wire with square cross-section is considered.

2.2 Simulation using variable separation method

2.2.1 Rectangular quantum wire

Initially SE (2.1) was solved assuming separation of variable for the wave-function ψ i.e., wavefunction along x-axis is independent to that of the one along y-axis. So,

$$\psi = \psi_x \psi_y \quad (2.2)$$

where ψ_x is the solution to the above SE (2.3) along x-axis, and similarly ψ_y is the solution to the above SE (2.3) along y-axis. Hence, solving the above 2-D Schrodinger's equation (2.1) (which is also a particular type of PDE (partial differential equation)) means solving the same SE for the 1-D case (which actually means solving for quantum well) twice and then extend it to 2-D using (2.2).

Time-independent Schrodinger's equation for one dimensional case is:

$$\frac{-\hbar^2}{2m^*} \frac{\partial^2 \psi}{\partial x^2} + V\psi = E\psi \quad (2.3)$$

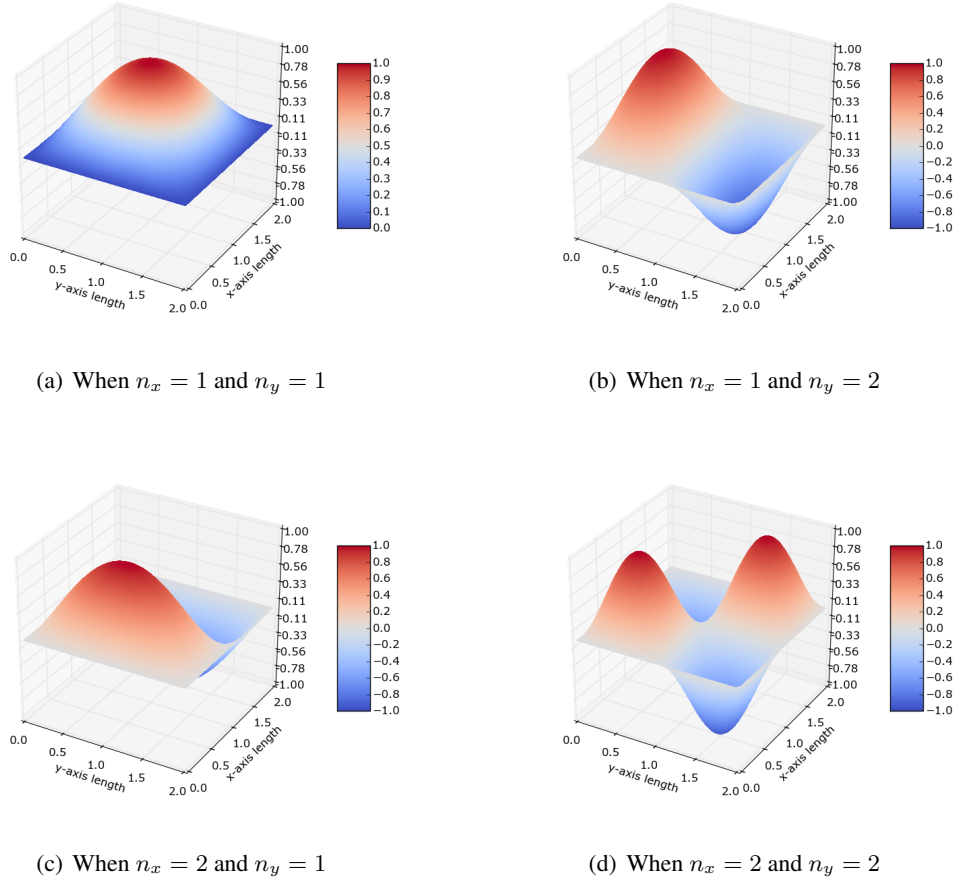


Figure 2.1: ψ for rectangular quantum wire at different energy levels

Solving SE (2.3) for the one-dimensional case is similar to solving an ODE (ordinary differential equation) with ψ as an unknown. So, for this, "odeint" function from the "scipy.integrate" module was used. This "odeint" function solves a system of ODEs using "lsoda" from the FORTRAN library odepack^{[7],[8]}. This is done for both x-axis and y-axis, thereby calculating ψ_x and ψ_y respectively. Each component is initialized, with $\psi_x, \psi_y = 0$ and $\frac{\partial \psi_x}{\partial x} = 1$ at one end i.e., when $x = 0$ or when $y = 0$ and using "odeint" function, SE (2.3) is solved for other region. Similar steps are repeated for the other component too.

Then, using the relation (2.2) and equations (2.1) and (2.3), ψ is calculated. The cross-section of the wavefunction ψ , perpendicular to the axis of the rectangular wire for different cases of n_x and n_y were calculated and are shown in fig 2.1.

Errors in the solution and its variation

The above solutions were verified with the wavefunctions ((2.4)) obtained by analytically solving the above SE (2.1). The analytical solution of 2.1 assuming separation of variables, i.e., 2.2 is:

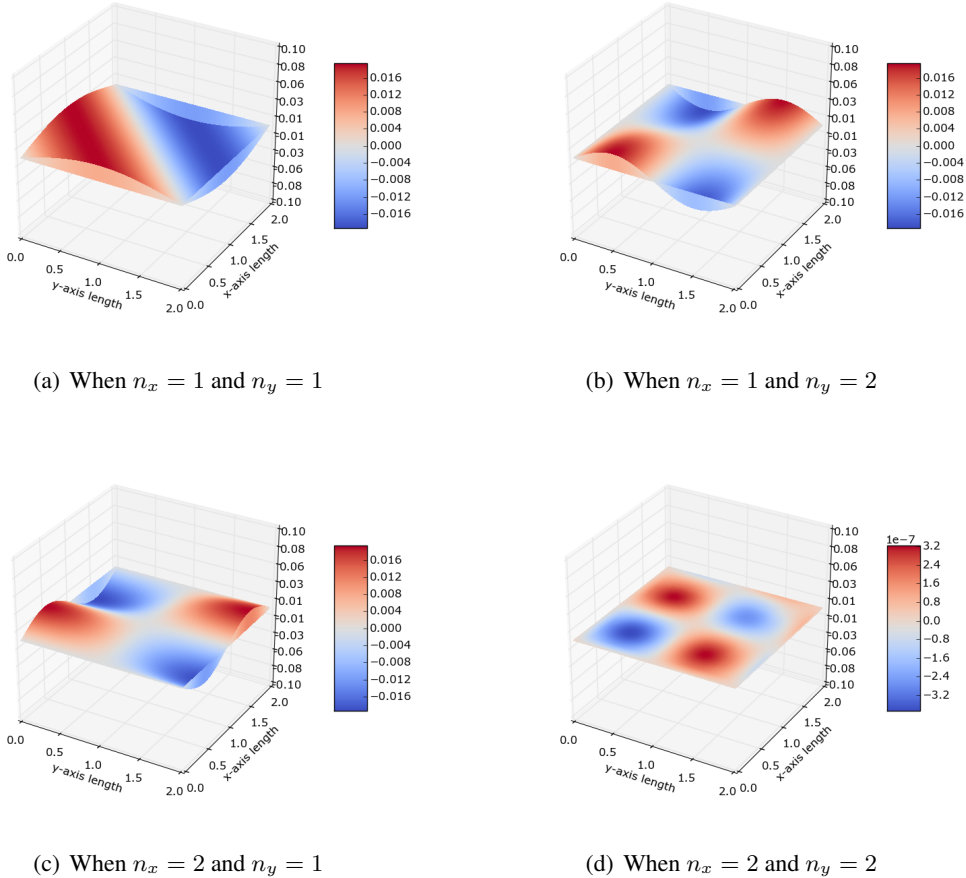


Figure 2.2: Relative error in ψ for rectangular quantum wire at different energy levels

$$\psi = \frac{2}{\sqrt{L_x L_y}} \sin\left(\frac{\pi n_x x}{L_x}\right) \sin\left(\frac{\pi n_y y}{L_y}\right) \quad (2.4)$$

Some slight variations could be observed due to various factors like the limitations in discretization, round-off errors, etc.

The relative error in ψ is plotted for the whole region in fig 2.2. It is actually, $\frac{\psi - \psi_{act}}{<|\psi_{act}|>}$, where $<|\psi_{act}|>$ is the absolute mean value of the actual wavefunction over the entire region. The errors indicate that calculated ψ value seem to have shifted a little towards $-ve$ x -direction and $-ve$ y -direction.

The mean error percentages and maximum error percentages obtained for the above numerical solutions when compared with the analytical solutions are shown in fig 2.3. This was done for various energy levels and for increasing number of blocks (discretization) i.e. smaller and smaller step sizes. They are shown in fig 2.3.

Overall the error decreases as the number of blocks increases, i.e. for decreasing step size. The error seems to drop down too low suddenly and return back to the trend when the number of blocks is a multiple of 4 and drops a lot more, if it is a multiple of 16. This is because the total length was 4 units and so when the number of blocks are multiples of 4, it means there are integer number of total blocks

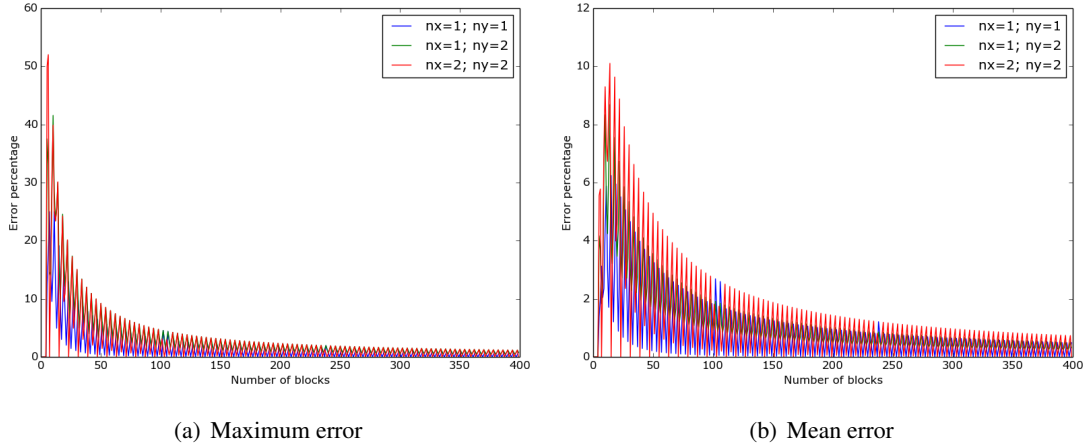


Figure 2.3: Error percentage variation

(i.e., integral frequency), thereby decreasing numerical errors. Errors reduce even more, for number of blocks that are multiples of 16 because of higher harmonics.

2.2.2 Circular quantum wire

The above solution for time-independent Schrodinger's equation (SE) (2.1) had only been solved for the rectangular coordinate system. That would be useful only for systems with rectangular symmetry, like square or rectangular quantum wire and cubical quantum dots. Whereas, for systems with radial symmetry like circular quantum wires, cylindrical and spherical quantum dots, SE should be solved in polar, cylindrical and spherical coordinate systems respectively. Two-dimensional SE (2.1) (assuming zero potential inside quantum wire region and infinite outside) in polar coordinate system could be written as:

$$-\frac{\hbar^2}{2m^*} \left[\frac{\partial^2 \psi}{\partial \rho^2} + \frac{1}{\rho} \frac{\partial \psi}{\partial \rho} + \frac{1}{\rho^2} \frac{\partial^2 \psi}{\partial \phi^2} \right] = \frac{\hbar^2 k^2}{2m^*} \psi \quad (2.5)$$

where $\psi \equiv \psi(\rho, \phi)$, and $k^2 = \frac{2m^* E}{\hbar^2} = \frac{j_{lm}^2}{R^2}$, R is the radius of the wire and $k_{lm} R = j_{lm}$ is the m^{th} zero of the l^{th} order Bessel function J_l .

Also, $m = n_r$ is the radial quantum number and $l = n_\phi$ is the angular quantum number.

Now, similar to the rectangular coordinate system case, the solution for the above equation is assumed to be independent along radial and angular directions i.e., solving SE (2.5) using separation of variables technique. That is,

$$\psi(\rho, \phi) = \psi_\rho(\rho) \psi_\phi(\phi) \quad (2.6)$$

Substituting equation (2.6) into equation (2.5), we get the following:

$$\psi_\phi \left[\frac{\partial^2 \psi_\rho}{\partial \rho^2} + \frac{1}{\rho} \frac{\partial \psi_\rho}{\partial \rho} + k^2 \psi_\rho \right] + \frac{\psi_\rho}{\rho^2} \frac{\partial^2 \psi_\phi}{\partial \phi^2} = 0$$

Now, dividing the whole equation by $\frac{1}{\rho^2} \psi_\rho \psi_\phi$, we get,

$$\frac{\rho^2}{\psi_\rho} \left[\frac{\partial^2 \psi_\rho}{\partial \rho^2} + \frac{1}{\rho} \frac{\partial \psi_\rho}{\partial \rho} + k^2 \psi_\rho \right] + \frac{1}{\psi_\phi} \frac{\partial^2 \psi_\phi}{\partial \phi^2} = 0$$

Here, the 1^{st} term, is independent of ϕ and similarly the second term is independent of ρ . But, they sum to zero. It means, the first and the second terms have to be equal to constants (that are independent of ρ and ϕ). Let those constants be l^2 and $-l^2$ respectively. Thus, we get the following two independent equations to be solved.

$$\frac{\rho^2}{\psi_\rho} \left[\frac{\partial^2 \psi_\rho}{\partial \rho^2} + \frac{1}{\rho} \frac{\partial \psi_\rho}{\partial \rho} + k^2 \psi_\rho \right] = l^2 \quad (2.7)$$

and

$$\frac{1}{\psi_\phi} \frac{\partial^2 \psi_\phi}{\partial \phi^2} = -l^2 \quad (2.8)$$

Simulation

For solving the above equations (2.7) and (2.8) numerically, the same Python *odeint* function, from the module *scipy.integrate* was used. It solves a system of ordinary differential equations using *lsoda* from the FORTRAN library *odepack*^[7]. This *LSODA*^[8], written by Alan Hindmarsh and L. R. Petzold, solves systems $\frac{dy}{dt} = f$ with a dense or banded Jacobian when the problem is stiff, but it automatically selects between non stiff (Adam's method^{[9]–[11]}) and stiff methods (BDF - Backward Differentiation Formula^[12]). It uses the non stiff method initially, and dynamically monitors data in order to decide which method to use.

The above equations (2.7) and (2.8) were first solved, with the above mentioned Python *odeint* function as follows:

First consider the case of finding ψ_ρ ,

$$\bar{y}_\rho = \begin{bmatrix} \frac{\partial \psi_\rho}{\partial \rho} \\ \psi_\rho \end{bmatrix} \text{ and } \frac{\partial \bar{y}_\rho}{\partial \rho} = \begin{bmatrix} \frac{\partial^2 \psi_\rho}{\partial \rho^2} \\ \frac{\partial \psi_\rho}{\partial \rho} \end{bmatrix} = \begin{bmatrix} \frac{(l^2 - \rho^2 k^2) \bar{y}_\rho[1]}{\rho^2} - \frac{\bar{y}_\rho[0]}{\rho} \\ \bar{y}_\rho[0] \end{bmatrix}$$

along with the initial conditions $\bar{y}_{\rho 0} = \begin{bmatrix} 0 \\ 1 \end{bmatrix}$ for $l > 0$, but $\bar{y}_{\rho 0} = \begin{bmatrix} 1 \\ 0 \end{bmatrix}$ for $l = 0$. Similarly, the process was repeated for ψ_ϕ ,

$$\bar{y}_\phi = \begin{bmatrix} \frac{\partial \psi_\phi}{\partial \phi} \\ \psi_\phi \end{bmatrix} \text{ and } \frac{\partial \bar{y}_\phi}{\partial \phi} = \begin{bmatrix} \frac{\partial^2 \psi_\phi}{\partial \phi^2} \\ \frac{\partial \psi_\phi}{\partial \phi} \end{bmatrix} = \begin{bmatrix} -l^2 \bar{y}_\phi[1] \\ \bar{y}_\phi[0] \end{bmatrix}$$

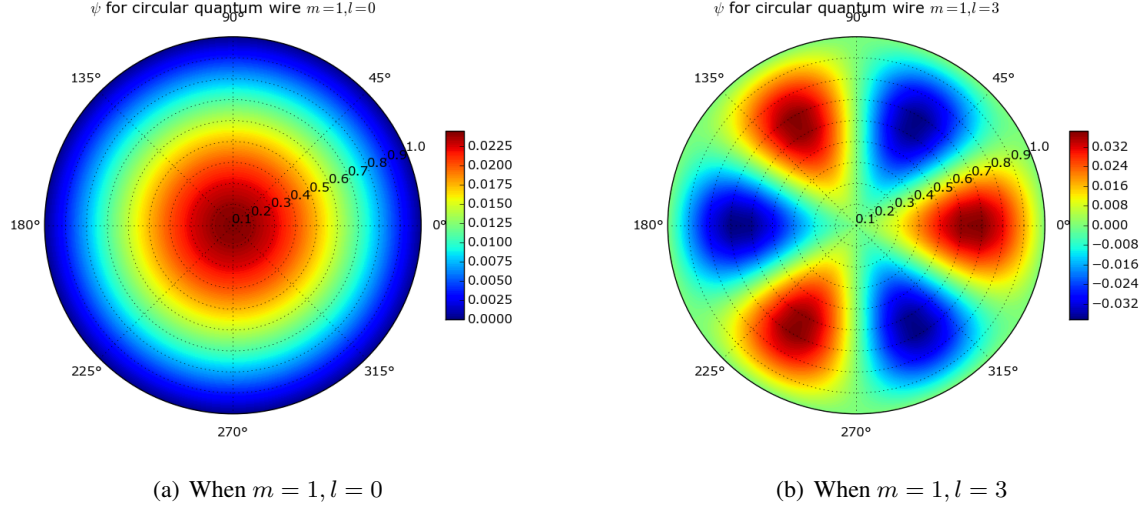


Figure 2.4: ψ for circular quantum wire when $m = 1$

with initial condition $\bar{y}_{\phi 0} = \begin{bmatrix} 0 \\ 1 \end{bmatrix}$. Basically, each component is initialized, say for $\psi_\rho, \psi_\rho = 0$ and $\frac{\partial \psi_\rho}{\partial \rho} = 1$ at one end i.e., at $r = 0$ and using "odeint" function, SE is solved for other region. Similar steps are repeated for the other component ψ_ϕ too. Then those solutions for ψ_ρ and ψ_ϕ were combined to get $\psi(\rho, \phi)$ from equation (2.6). Here, $k_{lm}R = j_{lm}$, where R is the radius of the wire and j_{lm} is the m^{th} zero of the l^{th} order Bessel function J_l .

One issue in the above procedure is that, the value of j_{lm} is unknown and should match with the actual value of j_{lm} . So, the simulation (involving just the ψ_ρ) was iterated for increasing values of j_{lm} from a continuous set of values. For each j_{lm} value, stationary state of the wavefunction is found and the simulation stops when the stationary state wavefunction has its m^{th} zero crossing at the boundary. The j_{lm} value got from the simulation, corresponding to this wavefunction matched very closely with the m^{th} zero of the l^{th} order Bessel function J_l . Thus, the simulated normalized wavefunction was expected to match with the analytical solution of the wavefunction. Hence, Bessel function is not explicitly assumed as the solution to ψ_ρ . Rather, it turns out to be so, confirming the correctness of the simulation. The wavefunctions are plotted in figures 2.4 and 2.5.

Errors in the solution and its variation

The analytical solution of 2.1 for circular symmetry systems, assuming separation of variables, i.e., 2.2 is:

$$\psi = \frac{1}{\sqrt{2\pi}} J_l(k_m r) \exp^{il\phi} \quad (2.9)$$

where l is azimuthal (angular) quantum number ($l = 0, \pm 1, \pm 2, \pm 3, \dots$) and k_m is related to m (radial quantum number). k_m is the m^{th} zero of the Bessel function of the first kind, $J_l(k_m r)$, i.e., $J_l(k_m R) = 0$, where R is the radius of the wire¹.

¹ Assuming $z = k_m r$, $\psi_\rho \equiv J_l(z)$ satisfies the equation $\frac{d^2 \psi_\rho}{dz^2} + \frac{1}{z} \frac{d\psi_\rho}{dz} + \left(1 - \frac{l^2}{z^2}\right) \psi_\rho = 0$

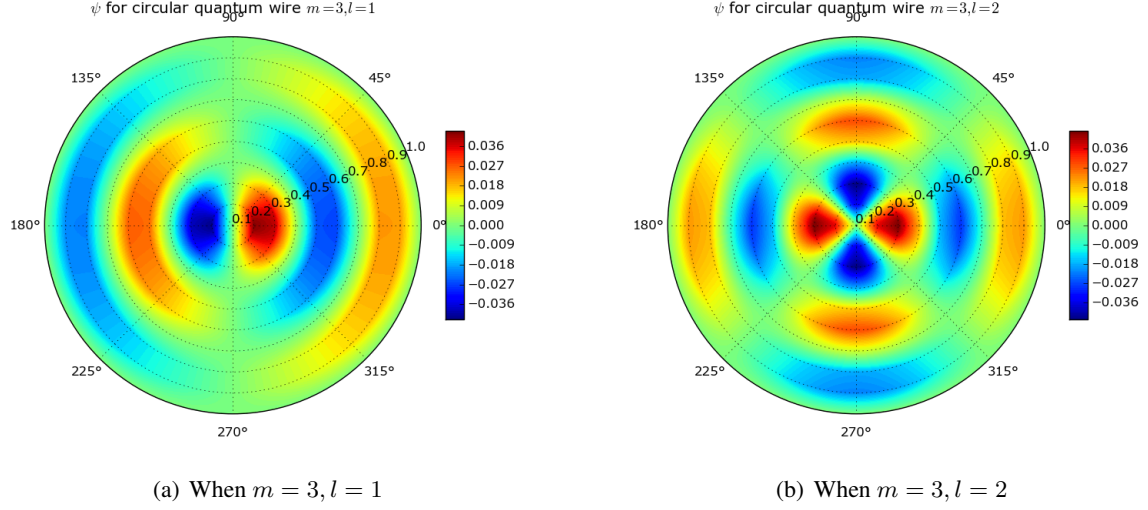


Figure 2.5: ψ for circular quantum wire with $m = 3$

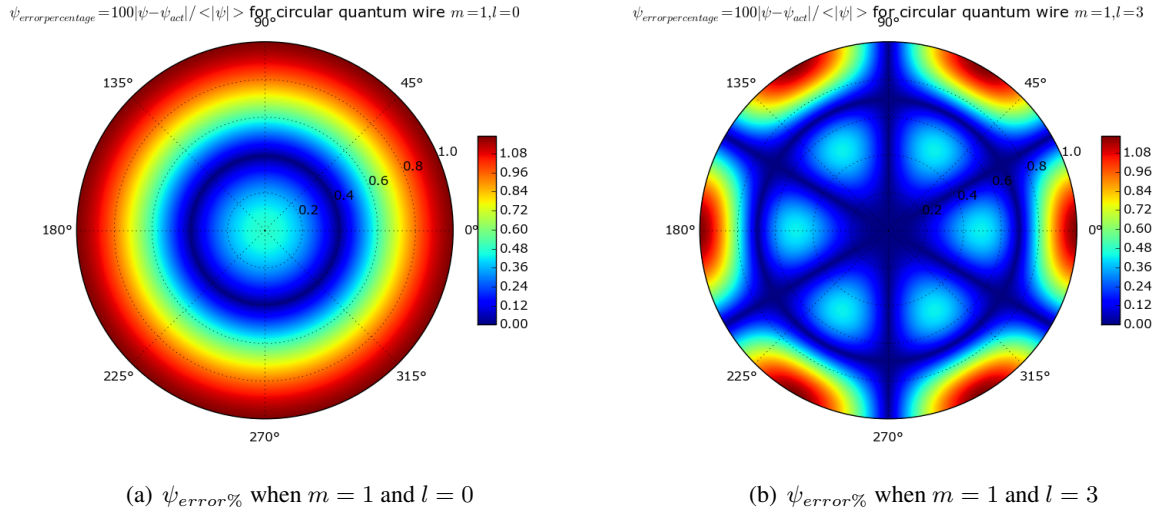


Figure 2.6: Error in ψ for circular quantum wire with $m = 1$

The absolute error of the wavefunction compared to the analytical solution ((2.9)) over the entire region is shown in figures 2.6 and 2.7.

The maximum and mean relative error percentages w.r.t. the mean value of ψ over the entire region for different l and m are tabulated in table 2.1. The relative error percentages w.r.t. the actual ψ value had computational difficulties. Anyway, it is similar to comparing the calculated values to $<\psi_{act}>$, which is the mean value of ψ over the entire region. In the earlier case, at the regions where ψ value goes to zero, the errors blow up unnecessarily. So, the error percentages were calculated by comparing with $<\psi_{act}>$ only. So, $\psi_{error\%} = \frac{|\psi - \psi_{act}|}{<|\psi_{act}|>} \times 100$. The calculated and the actual j_{lm} values and their relative error percentages are also tabulated in table 2.1.

The mean error is almost below 1% for all the above values of m and l . In the above simulations, one should note that, the grids were radial and angular and not rectangular. This causes an uneven spacing between the grid points causing errors increasing radially in the simulation.

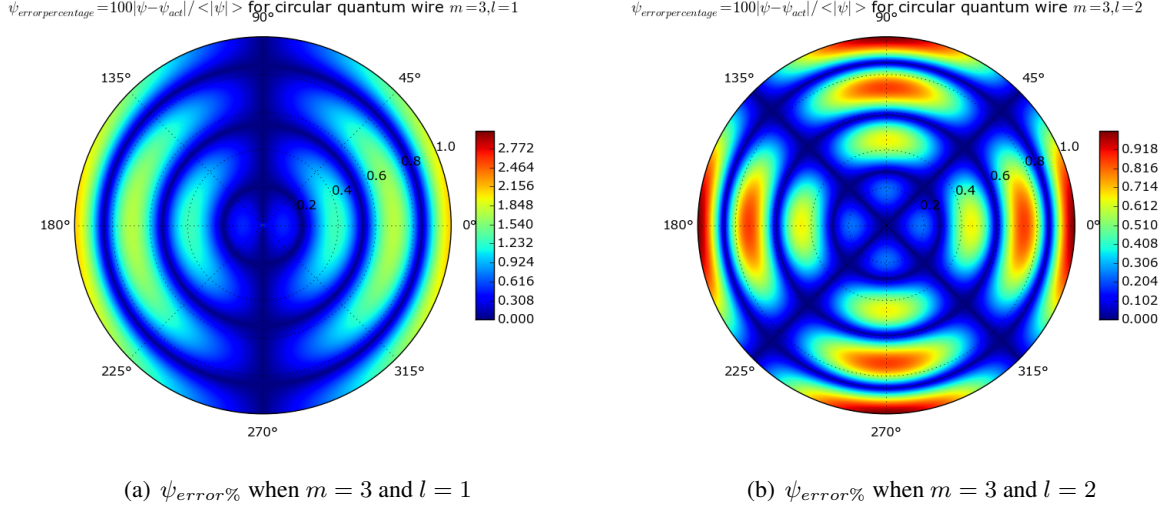


Figure 2.7: Error in ψ for circular quantum wire with $m = 3$

$abs(\psi_{calculated} - \psi_{act})$	Mean error %	Maximum error %	j_{lm}^{calc}	j_{lm}^{act}	$\Delta j_{lm} \%$
$m = 1, l = 0$	0.5340	1.1896	2.3908	2.4048	0.5822
$m = 1, l = 1$	0.2846	1.1538	3.8250	3.8317	0.1749
$m = 1, l = 2$	0.6676	3.1424	5.1198	5.1356	0.3077
$m = 1, l = 3$	0.2255	1.1844	6.3748	6.3802	0.0846
$m = 2, l = 0$	0.0686	0.1559	5.5182	5.5201	0.0344
$m = 2, l = 1$	0.1461	1.8326	7.0122	7.0156	0.0485
$m = 2, l = 2$	0.4492	1.8766	8.4066	8.4172	0.1259
$m = 2, l = 3$	0.8476	3.8027	9.7412	9.7610	0.2028
$m = 3, l = 0$	0.2891	0.6668	8.6456	8.6537	0.0936
$m = 3, l = 1$	0.5654	3.0544	10.1596	10.1735	0.1366
$m = 3, l = 2$	0.2548	1.0179	11.6137	11.6198	0.0525
$m = 3, l = 3$	0.3026	1.2723	13.0081	13.0152	0.0546

Table 2.1: Errors in the simulation

2.3 Simulation using finite difference method

In both the above cases of solving time-independent SE (2.1) in rectangular or polar coordinates, solution was assumed to be separable for either rectangular or cylindrical symmetry systems respectively. Similarly, variable separation method could be used to solve for ψ for systems with potentials of various symmetries^[13]. Now, for a general case we need to solve SE (2.1) for any arbitrary potential.

2.3.1 Rectangular quantum wire

The time-independent SE (2.1) in finite difference form for rectangular coordinate system would be:

$$\frac{\psi_{i+1,j} - 2\psi_{i,j} + \psi_{i-1,j}}{(\Delta x)^2} + \frac{\psi_{i,j+1} - 2\psi_{i,j} + \psi_{i,j-1}}{(\Delta y)^2} + k^2\psi_{i,j} = 0 \quad (2.10)$$

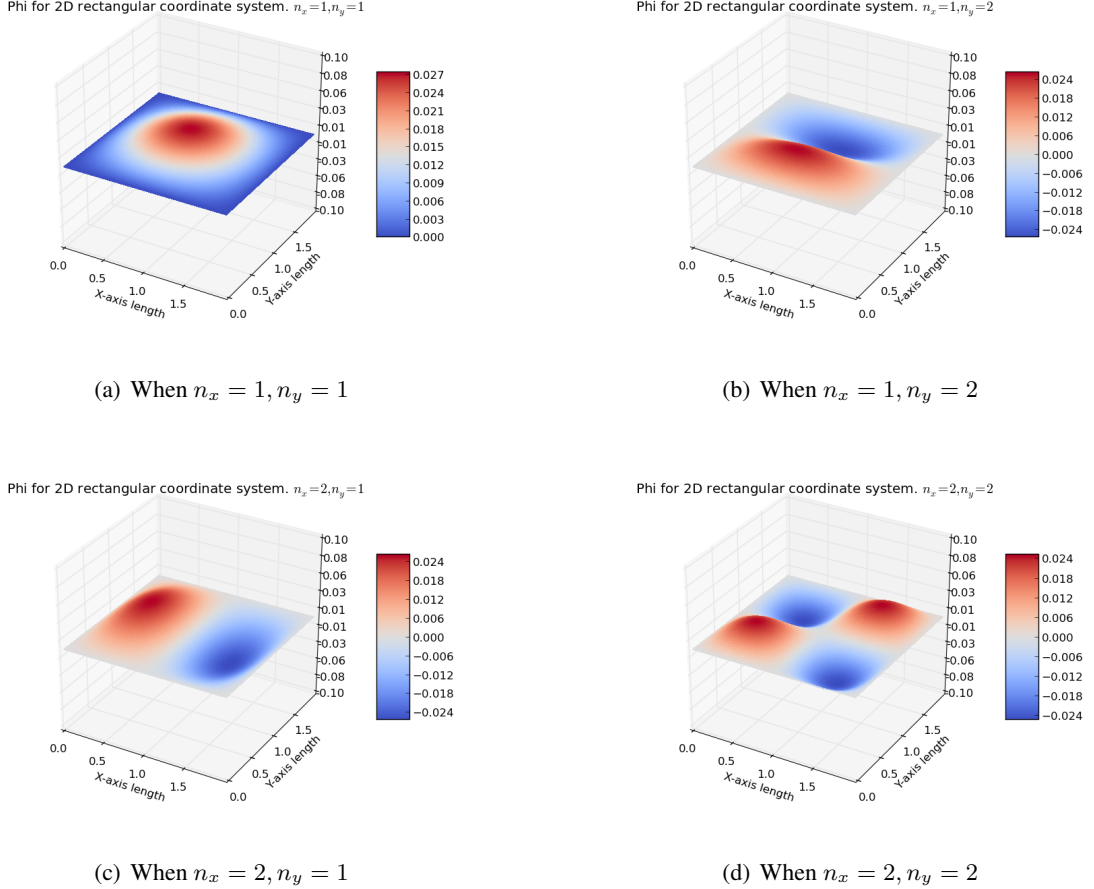


Figure 2.8: Normalized ψ for rectangular quantum wire at different energy levels

where $\psi_{i,j} \equiv \psi_{i,j}(x[i], y[j])$, and $k^2 = \frac{2m^*E}{\hbar^2} = k_x^2 + k_y^2$, $k_x = \frac{2\pi}{L_x}n_x$ and $k_y = \frac{2\pi}{L_y}n_y$. Here both L_x and L_y are divided into N pieces and for square quantum wire case $L_x = L_y$.

Based on the values of n_x and n_y , the wavefunction is initialized to $+1$ where the wavefunction is supposed to reach maximum and initialized to -1 where the wavefunction is supposed to reach minimum, i.e initialize symmetrically with $+1$ and -1 based on the values of n_x and n_y inside the wire region. Also, at the boundaries, ψ is maintained at 0 as long as the potential outside is infinite.

It is then solved by iterating many times, making sure of convergence. The central difference formulas are used here for solving SE (2.10).

Also, $\psi(\rho, \phi)$ has to be normalized for every iteration. So, $\psi = \frac{\psi}{\sqrt{\int_A dA \psi^* \psi}}$ so that $\int_A dA \psi^* \psi = 1$ is satisfied. In discrete sense, it means $\psi = \frac{\psi}{\sqrt{\frac{1}{A} \sum_{i,j} \psi_{i,j}^* \psi_{i,j}}}$ so that $\frac{1}{A} \sum_{i,j} \psi_{i,j}^* \psi_{i,j} = 1$ is satisfied, where A is the area of the wire region considered.

The normalized electron wave function after about 1000 iterations is plotted for different values of n_x and n_y in fig. 2.8.

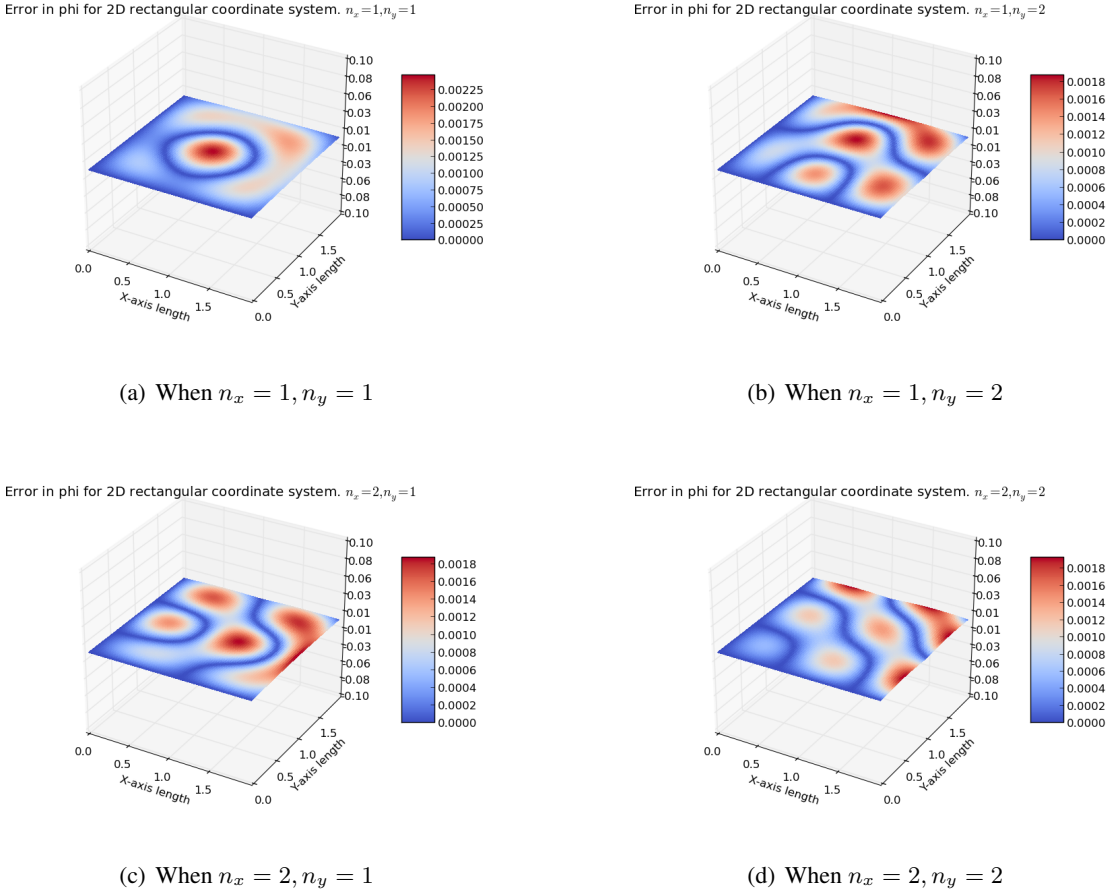


Figure 2.9: Error in ψ for rectangular quantum wire at different energy levels

Error in the solution and its variation

After normalizing $\psi_{i,j}$, it was compared with the analytical solution obtained from the variable separation method ((2.4)). The error which is the difference between the actual analytical solution and the solution got from the above analysis is shown in fig 2.9.

The figures in 2.9 show that the error is more at the regions where the ψ value itself becomes maximum. Also, close to one of the edges (and corners), the error becomes more, because, while numerically solving the Schrodinger's equation, the algorithm goes in one particular direction, thereby resulting in directional deviation in error.

The maximum and mean errors for different number of iterations for $n_x = 1$ and $n_y = 2$ is also plotted in fig 2.10. It is actually, the maximum and mean error of all values of ψ over the entire region for each iteration.

One can see that both the maximum and mean error decreases as the number of iterations increases. This shows that the solution is actually converging, which means that the simulation was stable.

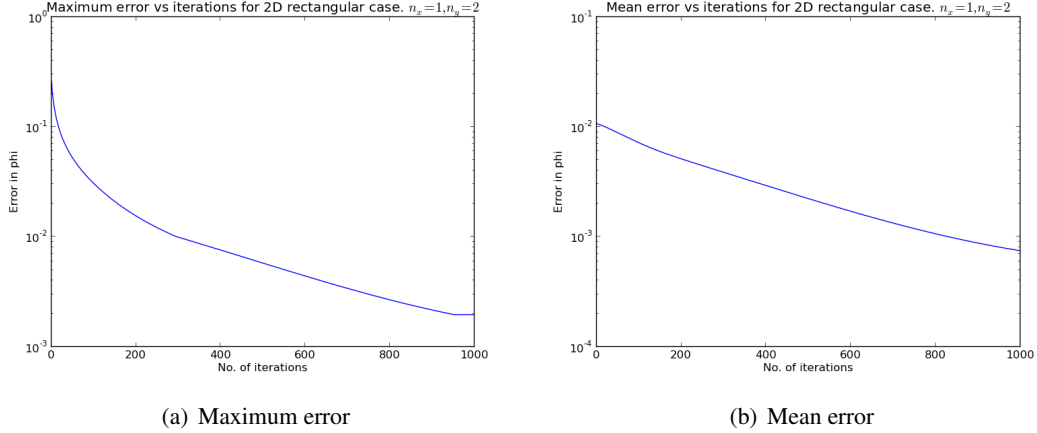


Figure 2.10: Maximum and mean error in ψ for different no. of iterations, for rectangular quantum wire when $n_x = 1, n_y = 2$

2.3.2 Circular quantum wire

The time-independent SE (2.1) in finite difference form for polar coordinate system would be:

$$\frac{\psi_{i+1,j} - 2\psi_{i,j} + \psi_{i-1,j}}{(\Delta\rho)^2} + \frac{\psi_{i+1,j} - \psi_{i-1,j}}{2(\Delta\rho)\rho_i} + \frac{1}{\rho_i^2} \frac{\psi_{i,j+1} - 2\psi_{i,j} + \psi_{i,j-1}}{(\Delta\phi)^2} + k^2\psi_{i,j} = 0 \quad (2.11)$$

where, $(\rho_i, \phi_j) \equiv (i, j)$ and $1 \leq i \leq M; 1 \leq j \leq N$, because radius of the (quantum) wire was divided into M pieces and angle (here totally it is 2π) into N pieces.

Based on the values of n_ρ or m and n_ϕ or l , the wavefunction was initialized to $+1$ where the wavefunction was supposed to reach maximum and initialized to -1 where the wavefunction was supposed to reach minimum, i.e initialize symmetrically with $+1$ and -1 based on the values of n_ρ and n_ϕ inside the wire region. Also, at the boundaries, ψ was maintained at 0 as long as the potential outside was infinite.

Similar to the rectangular quantum wire case, here too $\psi_{i,j}$ was normalized every iteration and convergence of the solution was checked.

The normalized electron wave function after about 1000 iterations is plotted for different values of $n_\rho = m$ and $n_\phi = l$ in fig 2.11.

Error in the solution and its variation

After normalizing $\psi_{i,j}$, it was compared with the analytical solution obtained from the variable separation method ((2.9)). The error which is the difference between the actual analytical solution and the solution got from the above analysis is shown in fig 2.12.

Similar to the rectangular coordinate case, the errors reach maximum values, mostly in the regions

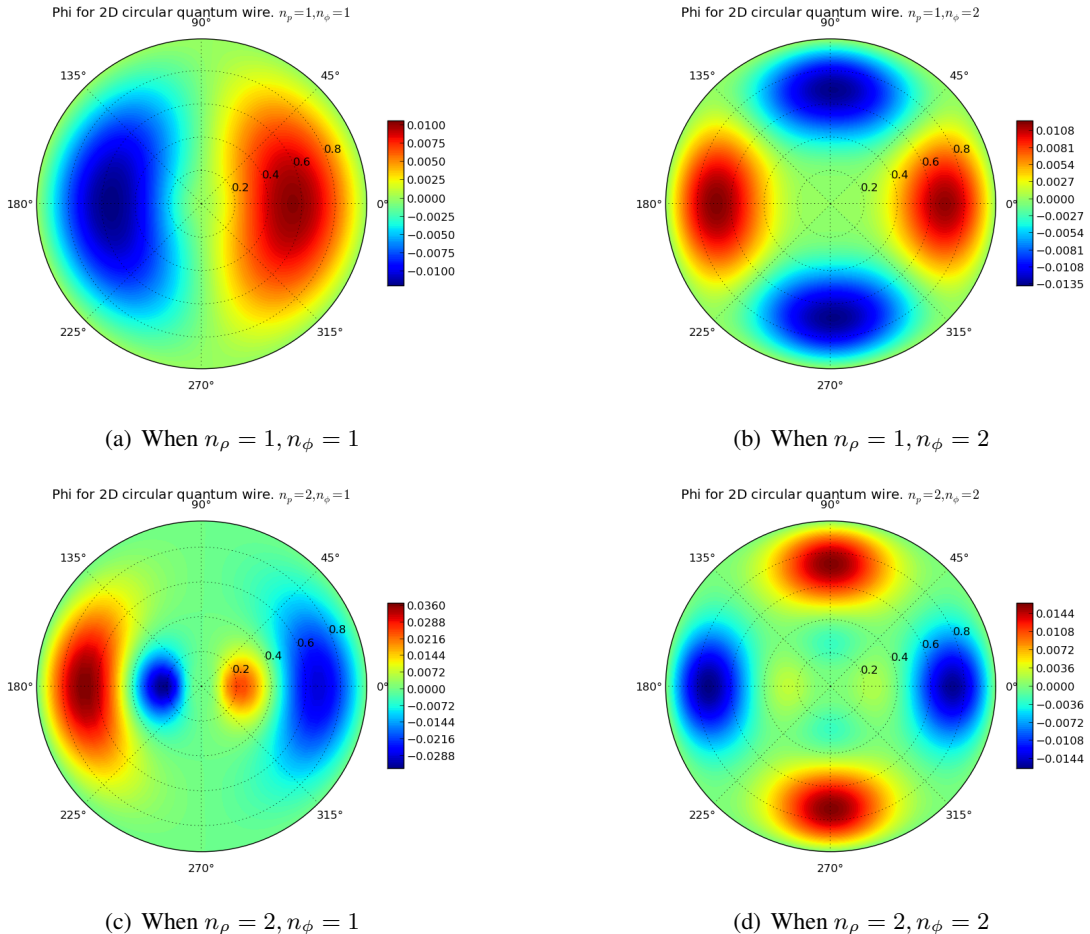


Figure 2.11: Normalized ψ for circular quantum wire at different energy levels

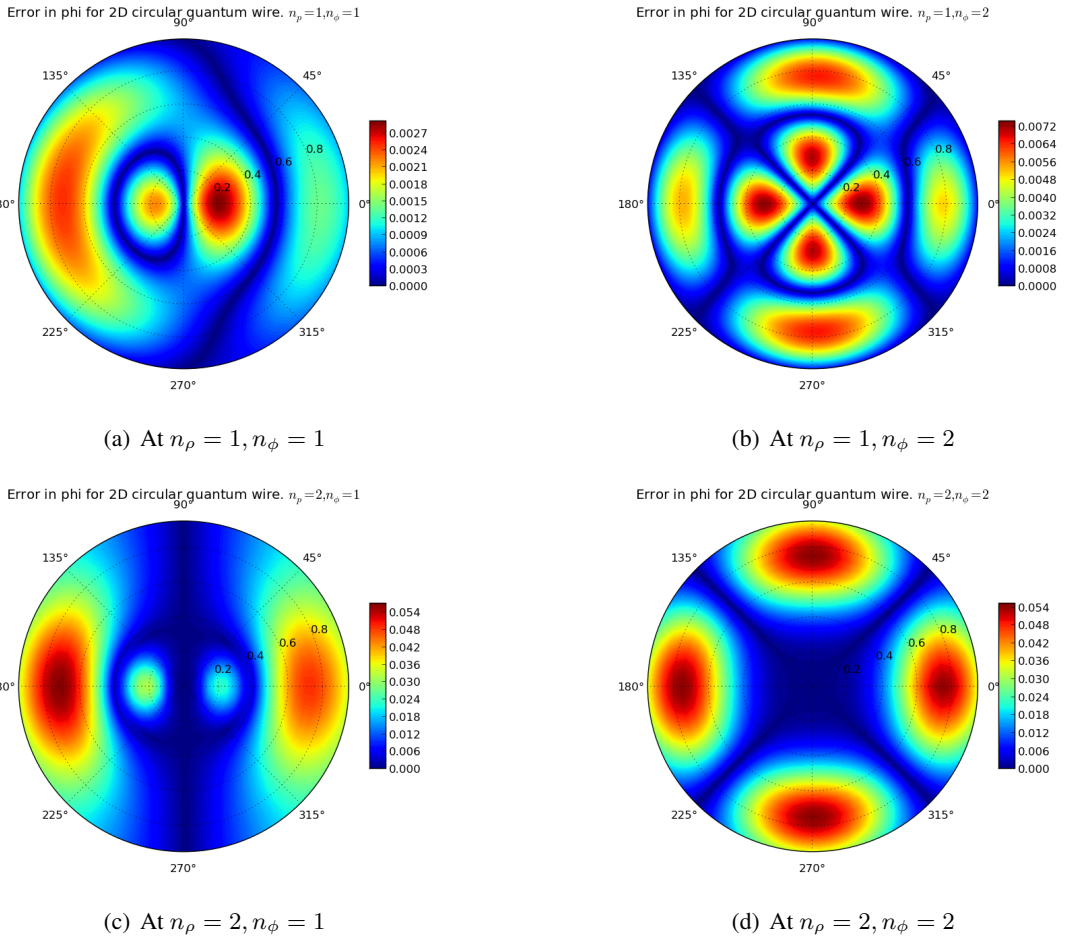


Figure 2.12: Error in ψ for circular quantum wire at different energy levels

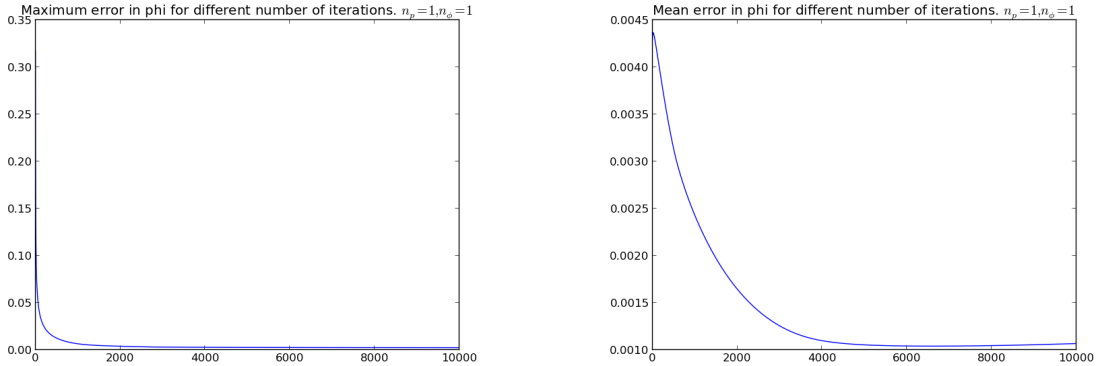


Figure 2.13: Maximum and mean error in normalized ψ for circular quantum wire at $n_\rho = 1, n_\phi = 1$

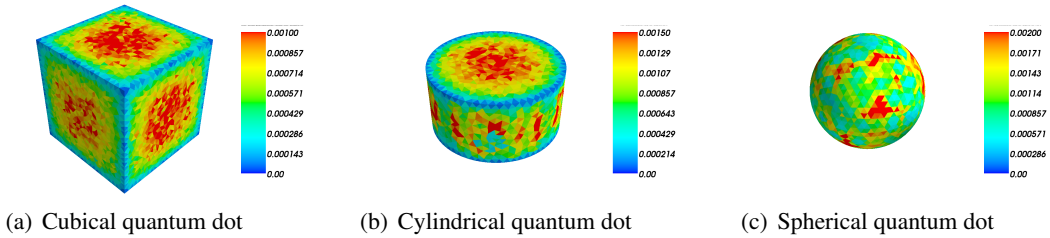


Figure 2.14: Normalized ψ for quantum dots - ground state

where ψ itself reaches maximum value. But, at some regions there is asymmetry in the errors caused, which could possibly be because of the directional preference of the algorithm being used for numerically solving the Schrodinger's equation.

The maximum and mean errors for different number of iterations for $n_\rho = m = 1$ and $n_\phi = l = 1$ are also plotted. They are actually the maximum or mean error of all values of ψ over the entire region for each iteration.

Both the maximum and mean error decreases as the number of iterations increases, similar to the previous case with rectangular coordinate system. This shows that the solution was actually converging and the simulation was stable for polar coordinate system too (fig 2.13).

2.4 Simulation of quantum dot using mesh-based methods

Simulation of quantum wires and dots for complicated potentials could also be done using PDE solver with a mesh. A mesh is generated for a required geometry using *Gmsh* software - it is a 3D finite element grid generator with a build-in CAD engine and post-processor. Then, SE (2.1) is solved for this geometry using *FiPy* - an object oriented, partial differential equation (PDE) solver, written in Python, based on a standard finite volume (FV) approach. Finer meshing not only gives more accurate solution, but also the ease to visualize better. The wave function was normalized using: $\psi = \frac{\psi}{\sqrt{\int_S ds \psi^* \psi}}$, where ds = differential area or volume of the entire range. The ground state wavefunctions of quantum dots are shown using *Mayavi2* (3D) data visualizing software in fig 2.14.

2.5 Simulation using LOBPCG method

The time-independent 3D Schrodinger's equation (SE) for a quantum wire is,

$$-\frac{\hbar^2}{2m^*} \left[\frac{\partial^2 \psi}{\partial x^2} + \frac{\partial^2 \psi}{\partial y^2} + \frac{\partial^2 \psi}{\partial z^2} \right] = (E_{2D} + E_z) \psi \quad (2.12)$$

where the total energy is given by, $E_{tot} = E_{2D} + E_z$. Due to 2D confinement, the quantum wire allows only a certain discrete set of energy modes to exist. The corresponding energies E_{2D} of each mode are actually the eigen values of SE (2.1) (because SE (2.1) is an eigen value equation). For now, it is assumed that $V = 0eV$ inside the wire region and infinite outside. Thus E_{2D} takes values from only a finite set of values (eigenvalues) depending upon the various modes of the wavefunction ψ . Also, assuming total energy, $E_{tot} = E_F$ to be constant, where E_F is the Fermi energy. Then it means that E_z is also restricted to take only a finite set of values. This means, while considering electron flow through a nanowire (along its axis), only certain modes can pass through, thereby modifying a lot of current-based parameters in comparison to the corresponding parameters in planar layers.

The eigen values of SE (2.1) are the eigen energies of the different eigen modes allowed inside the wire region and the wavefunction ψ is given by the eigen vectors of the same equation. These eigen vectors and values are modified due to various parameters. The variations in the following cases are studied here. When,

- size of the quantum wire is changed
- 4 quantum wires arranged in a lattice are considered
- potential outside the 4 quantum wires is varied
- gap between the 4 quantum wires is varied

Here, the wavefunction is initialized with random values over the entire region of interest (here just the wire region) whereas at the boundaries it always remains at zero because, of infinite potential. The Schrodinger's equation (2.1) is solved using a smoothed aggregation solver^[14] with the help of some preconditioners. The eigen value equation was solved by LOBPCG^{[15],[16]} (Locally Optimal Block Preconditioned Conjugate Gradient) method. This was implemented using python-based PyAMG (Algebraic Multi-Grid solver) libraries.

2.5.1 Eigen energy levels of a rectangular quantum wire

The first 9 energy levels of a square quantum wire is shown in fig 2.15. The size of the quantum wire is assumed to be $l_w = 10nm$. The wavefunctions of the degenerate levels are actually orthogonal to each other, i.e. ψ_1 and ψ_2 satisfy $\int_A dA \psi_1^* \psi_2 = 0$, which in discrete form is $\sum_{i,j} \psi_1^{i,j*} \psi_2^{i,j} = 0$. So, if we assume separation of variables, then we get the following wavefunction pairs for the degenerate energy levels.

From figure 2.16, the degenerate energy level pairs are 1 ($n_x = 2$ and $n_y = 1$) and 2 ($n_x = 1$ and $n_y = 2$); 4 ($n_x = 1$ and $n_y = 3$) and 5 ($n_x = 3$ and $n_y = 1$); 6 ($n_x = 3$ and $n_y = 2$) and 7 ($n_x = 2$

and $n_y = 3$). Here n_x and n_y are respectively the $x - axis$ and $y - axis$ quantum numbers when the separable wavefunctions are considered for simulation.

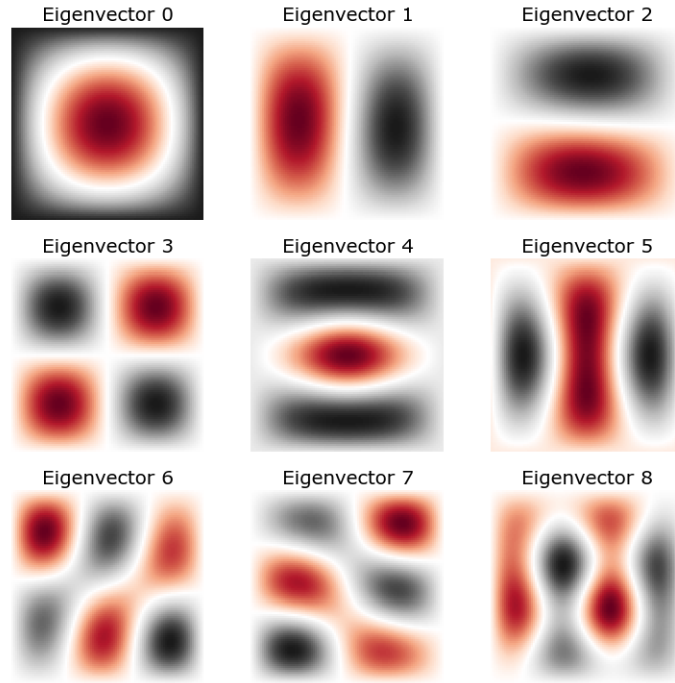


Figure 2.15: First 9 eigen energy levels of a square quantum wire

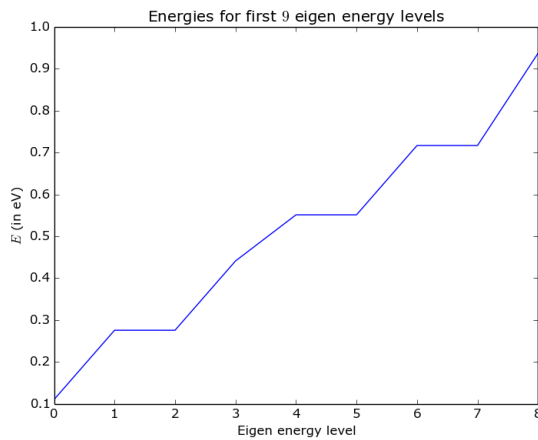


Figure 2.16: Eigen energies (in eV) of a square quantum wire for first 9 energy levels

In fig 2.15, *red* colour represents *+ve* values of about 10^{-2} in magnitude and similarly *black* colour represents *-ve* values of similar magnitude, whereas *white* colour represents values that are comparatively very close to zero (about $\pm 10^{-5}$). The same colour mapping is followed for later plots too. The wavefunctions ψ that are plotted in 2.15 are the first 9 eigen vectors of 2D SE 2.1. Here, for any eigen vector, if Ψ is an eigen vector with an eigen value energy of say, E_Ψ , then for the same eigen energy

value, $-\Psi$ is also an eigen vector. So, since the wavefunction was initialized to random values initially, for each level, we end up getting either $+\Psi$ or $-\Psi$, which is clear from 2.15, where sometimes the surrounding is *red -ve* or *black +ve*. The eigen energies obtained using *LOBPCG* method is shown in fig 2.16. They are very close to the analytical values: $E_{2D} = \frac{\hbar^2(k_x^2+k_y^2)}{2m^*} = \frac{\hbar^2\pi^2(n_x^2+n_y^2)}{2m^*L_x^2}$, assuming $L_x = L_y$ and m^* is the effective mass of an electron in a *GaAs* crystal. It is $m^* = 0.067m_0$, where m_0 is the rest mass of an electron.

2.5.2 Eigen energies for wires of different dimensions

The energy eigenvalues of the first 10 energy levels are shown here, as the size (l_w) of the square quantum wire was varied from $0.1nm$ to $20nm$ (figure 2.17). As seen earlier in the figure 2.16, some of the energy levels are degenerate, i.e., have same energy for all wire sizes. For example, the energy level 1 with $n_x = 2$ and $n_y = 1$ has same energy as the energy level 2 with $n_x = 1$ and $n_y = 2$.

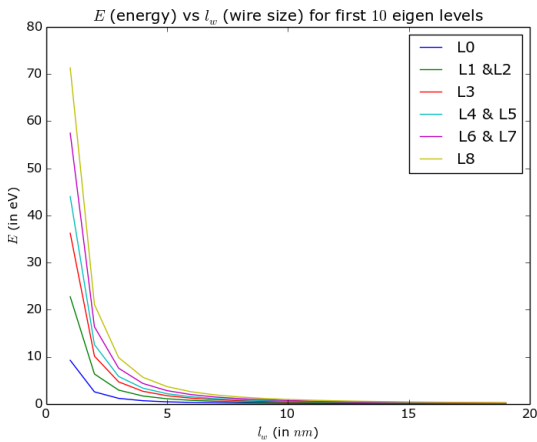


Figure 2.17: E_{2D} (in eV) vs l_w ($\times 10^{-10}$ m)

All the eigen energies E_{2D} shown here decrease as the wire size l_w increases. This is because, $E_{2D} = \frac{\hbar^2}{2m^*} \left(\left(\frac{2\pi n_x}{L_x} \right)^2 + \left(\frac{2\pi n_y}{L_y} \right)^2 \right)$. So, $E_{2D} \propto \frac{1}{l_w^2}$, because $L_x = L_y = l_w$.

2.5.3 Eigen energy levels of an array of 4 quantum wires

Now similarly, the first 9 eigen energy levels (figure 2.18) for the case when there is an array of 4 quantum wires placed in a crystal lattice equally spaced from each other. Here, the size of each of the square quantum wires is $l_w = 2nm$ and the lattice width considered is about $10nm$. The space between the rectangular wires is also $2nm$. The potential considered outside the wire region is not infinite, but rather a finite value of $V = 10eV$. Whereas, as usual zero potential is considered inside the wire region and infinite potential outside the lattice. So, at the lattice boundaries, the wavefunction goes to zero. The wavefunction is initialized with random values over the entire lattice region and the SE (2.1) is solved in a way explained earlier in the beginning of this section. Unlike the single wire case, for the 4 wires case the first 4 energy levels are degenerate, whereas in the single wire case, 2nd and 3rd levels only are the

first set of degenerate levels and only two levels are degenerate, i.e. with same energy. Whereas, in the case with 4 wires, the next 5 energy levels are degenerate (fig 2.19). The colour map used here is similar to the one mentioned in section 2.5.1.

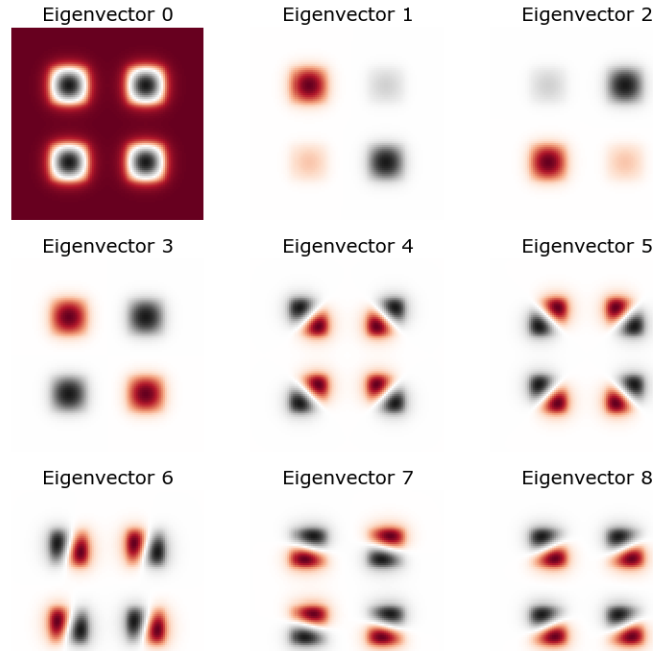


Figure 2.18: First 9 eigen energy levels of 4 quantum wires

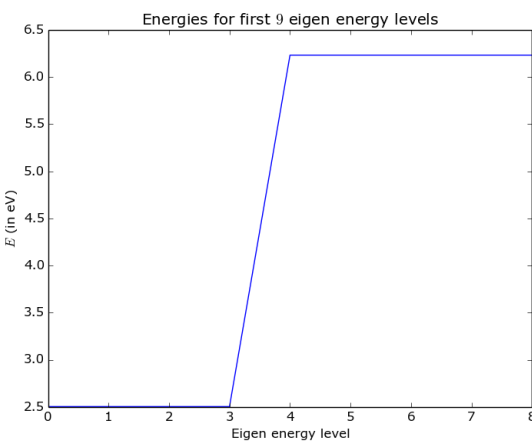


Figure 2.19: Eigen energies (in eV) of a square quantum wire for first 9 energy levels

2.5.4 Variation of eigen energies due to outside potential

Using different materials as substrate means different Fermi energies, therefore different potentials in the lattice, outside the wire region, compared to the potential inside the wire, for a particular material of

wire. So, the variation of the eigen energies is studied as the potential outside $V_{outside}$ is changed. Here, the potential outside the lattice is always infinite and potential inside the wire region is zero, but $V_{outside}$ which is the potential outside the wire and in the lattice is varied. It is varied from 0eV to 4eV . The case $V_{outside} = 0\text{eV}$ is same as considering the whole lattice region as one single wire region. Also, like the previous case, the wire size and the gap between the wires is maintained at 2nm and the size of the lattice region considered is also maintained at 10nm .

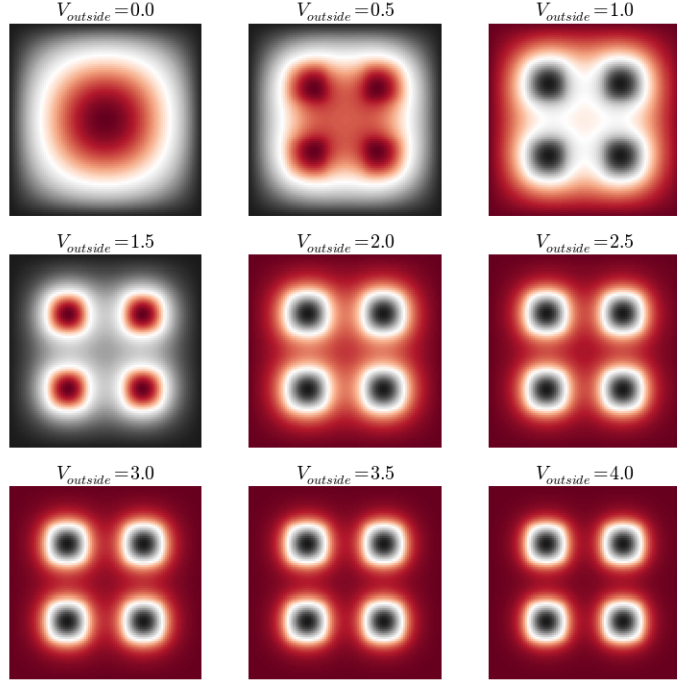


Figure 2.20: Ground state energy for different $V_{outside}$ (in eV)

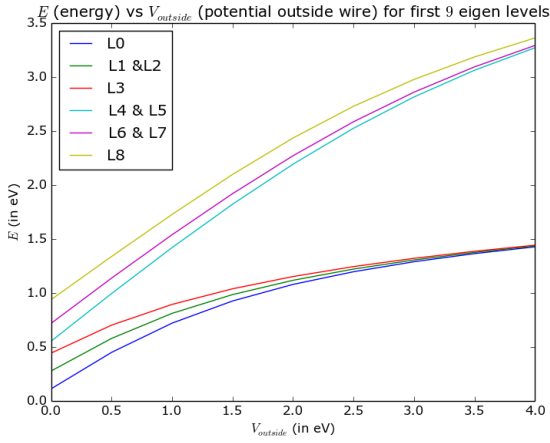


Figure 2.21: E_{2D} (in eV) vs $V_{outside}$ (in eV) for first 9 eigen energy levels

The colour map used here is similar to the one mentioned in section 2.5.1. At lower potentials, the

wires interfere with each other significantly (figure 2.20). The first 4 energy levels which are very distinct for $V_{outside} = 0eV$ (because it is similar to a quantum wire of size $l_w = 10nm$) become degenerate as the potential outside becomes larger compared to the potential inside. Similarly, the next 5 energy levels also become degenerate as $V_{outside}$ increases. Also, all the eigen energies monotonically increase (from fig 2.21) as $V_{outside}$ increases. This is because, as $V_{outside}$ is close to $0eV$, it is similar to considering one single quantum wire of size $l_w = 10nm$, whereas when $V_{outside}$ is about $4eV$ and higher, then most of the electron wavefunction is localized inside the wire regions of the 4 quantum wires, each of which is of size $l_w = 2nm$. So, effectively, there is a decrease in the apparent wire size considered. In section 2.5.2, it was shown that eigen energies increased drastically as the wire size decreased, which explains the above behaviour of the eigen energies with respect to $V_{outside}$.

2.5.5 Eigen energy levels as the gap between the 4 wires is varied

In the previous two subsections (2.5.3 and 2.5.4), the simulation was carried out assuming that there are 4 rectangular quantum wires of same size of $l_w = 2nm$ which are placed apart from each other with some gap, in a crystal lattice of size $10nm$. Now, the change in the eigen energies of the system is studied as the gap between the wires is varied from $6nm$ to $0.4nm$. The potential outside the wire region is kept constant for the entire simulation, $V_{outside} = 10eV$ compared to the zero potential inside the wire region.

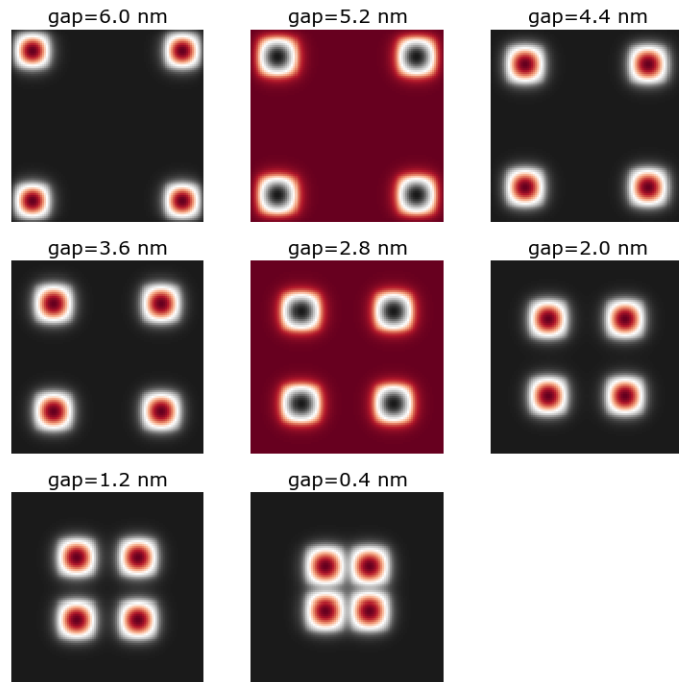


Figure 2.22: Ground state energy for different gaps (in nm) between the wires

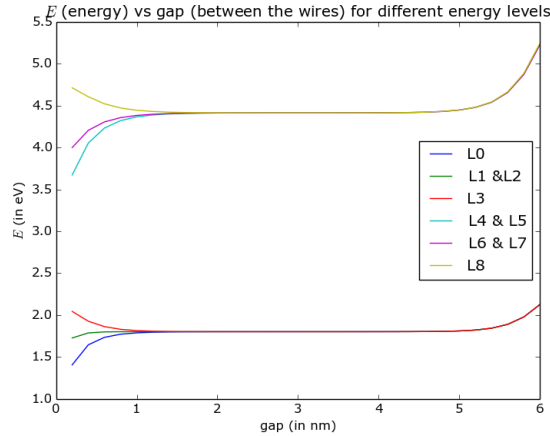


Figure 2.23: E_{2D} (in eV) vs gap between the wires (in nm) for first 9 eigen energy levels

The colour map used here is similar to the one mentioned in section 2.5.1. The eigen energies are almost same, mostly (fig 2.22). Only when the gap between the wires is closer than half the size of the wire (here about 1nm), the system behaves as if there is a single larger wire in the centre, because of lateral quantum tunneling between the wires (fig 2.23). Also when the gap between the wires is so much that the wires are about half the wire size distance (here about 1nm) from the boundaries (of the lattice), the eigen energies increase because the electrons get reflected from the infinite lattice boundaries and need more energy to stay confined in the wires close to the boundaries (fig 2.23).

CHAPTER 3

Tunneling Magneto Resistance

3.1 Theory and importance of TMR

3.1.1 Spin of an electron

Spin is an intrinsic property of elementary particles and participates in magnetic interactions. An electron is an elementary particle that carries a negative electric charge $-e$ and a spin $1/2$ corresponding to the magnetic moment of $e/(2mc) = 9.285 \times 10^{-24} (JT^{-1})$. We cannot separate a spin from a charge when we deal with electrons. When the electric current flows in a wire, both charge and spin are carried by electrons. In contrast to the electric charge, the spin of an electron has two directions, up or down. In nonmagnetic conductors such as *Cu*, *Al*, and *Au*, spin-dependent phenomena are not observed, since the same number of spin-up and spin-down electrons are present. However, in magnetic materials such as *Fe*, *Co*, and *Ni*, the number of electrons with spin up is different from that with spin down. Therefore, the transport properties of magnetic materials are spin dependent. We can vary the resistance by applying a magnetic field to change the direction of magnetization. This phenomenon is called magnetoresistance (MR) and is applied to magnetoresistive devices such as hard-disk drives. Electron tunneling is a basic phenomenon in quantum mechanics by which electric current can pass from one electrode through a thin insulating barrier layer into a second electrode. Recently, spin-dependent tunneling in magnetic tunnel junctions has attracted enormous attention because of its potential applications in high-density magnetic recording devices and nonvolatile magnetic random access memory (MRAM). Spin-dependent tunneling is also important from a scientific point of view, since it provides much information about the physical properties of magnetic materials^[17].

3.1.2 TMR of magnetic tunnel junctions

Two ferromagnetic metals separated by an insulating oxide layer exhibit a giant magnetoresistance^{[18],[19]} of up to 40% due to tunneling across the insulating layer. The tunneling magnetoresistance TMR effect was observed by Julliere^[20] (see also Maekawa and Gafvert^[21]) but the magnitude of the TMR in these early experiments was very small. Theoretical interpretation of the TMR effect has been based on the conventional theory of tunneling see, for example, Refs. [22] and [23]. The main conclusion of the conventional theory of tunneling is that the tunneling current is proportional to the product of the densities of states in the left and right electrodes. This conclusion is arrived at by treating tunneling as a quantum transition from one electrode to the other. The two electrodes between which the transitions take place are regarded as two separate systems described by different Hamiltonians^[24]. Such a separation is clearly impossible in the closely related problem of the current perpendicular-to-plane giant magnetoresistance CPP GMR since the two ferromagnets are strongly coupled in the metallic regime

via a nonmagnetic metallic spacer. Given that the CPP GMR and TMR seem to require different theoretical treatment, one might conclude that they are qualitatively different effects. It is, therefore, rather remarkable that the observed magnitudes of the CPP GMR and TMR are comparable despite the fact that the individual resistances of a tunneling junction in its ferromagnetic and antiferromagnetic configurations are several orders of magnitude higher than those of a metallic trilayer. Experimentally, the two effects seem to be closely related. To establish a theoretical link between the TMR and CPP GMR, it is necessary to develop a nonperturbative theory of tunneling that treats the two electrodes together with the tunneling barrier as a single quantum-mechanical system. This is, indeed, the method one uses to solve the textbook problem of tunneling through a rectangular barrier. The rectangular barrier model was already applied by Slonczewski^[25] to calculate the TMR^[26].

3.1.3 Theories explaining TMR

In the early studies on spin-dependent tunneling, the theoretical interpretation was based on a simple model in which the spin is conserved in the tunneling process and the conductance of each spin direction is proportional to the densities of states of that spin in each electrode. In this model, the tunnel current is larger when the magnetizations of the two electrodes are parallel than when they are antiparallel, which explains the strong dependence of the tunneling current on the relative orientation of the magnetizations of the ferromagnetic electrodes. However, the model does not explain the experimental results that the TMR exhibits rather large bias and temperature dependencies. Another approach based on the single-electron Schrodinger equation was proposed by Slonczewski^[25] (1989). By extending the free-electron model of tunneling in nonmagnetic tunnel junctions^[27] to magnetic tunnel junctions, Slonczewski found that the polarization of tunneling electrons depends not only on the electronic density of states of FMs but also on the potential height of the tunnel barriers^[25]. In this approach, the electrodes and the insulating barrier are treated as a single quantum-mechanical system and the wave functions of up and down electrons are constructed by solving the Schrodinger equation in the whole system. While the free-electron model captures some essential features, their predictions for TMR are quantitatively unreliable because the lattice structure of the electrodes and the variation of the band structure near the insulating barrier are overlooked^[28]. The tight-binding model gives more realistic descriptions for TMR. This approach allows one to distinguish electronic structures at interfaces from that in the bulk and to study the effect of the interface roughness, although it contains some empirical parameters. One can easily see that the single-band tight-binding model reduces to the free-electron model. It is also shown that the conductance of the tight-binding method reduces to the usual expression for the conductance obtained in the classical theory of tunneling when the electron hopping between the electrodes is weak and the coherence across the barrier is completely lost^[17].

3.1.4 Free electron model

In the tunnel Hamiltonian model in the preceding section, we assumed that the tunneling matrix elements and the spin-up and spin-down electrons can be treated as constants. In other words, the wave function in the barrier region is assumed to be independent of the wave vector and spin. However, it is not obvious that the above assumptions are justified. In 1989, Slonczewski proposed another approach

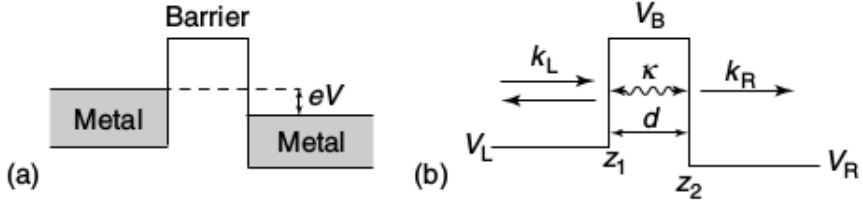


Figure 3.1: (a) Potential energy diagram for a metal/insulator/metal tunnel junction with the bias voltage V (b) The geometry of one-electron potential

for the spin-dependent tunneling based on the free-electron model, where the exact wave function in the barrier region is used^[25] (Slonczewski, 1989). He showed that TMR is determined not only by the spin polarization of FM electrodes, P , but also by the potential height of the insulating barrier. Introducing the effective spin polarization of the ferromagnetic electrode, P_{eff} , which ranges from $-P$ to P depending on the potential height of the barrier, the TMR is expressed using the same formula as that derived from the tunnel Hamiltonian model. Before studying the spin-dependent tunneling in ferromagnetic tunnel junctions, it is convenient to consider the nonmagnetic tunnel junctions and derive an approximate form of the tunnel conductance in weak transmitting limit^[27] (Burstein and Lundqvist, 1969). When the bias voltage V is applied, electrons incident from the left electrode tunnel through the insulating barrier, resulting in a tunnel current, as shown in fig 3.1. The shaded area represents the occupied states of electrons at zero temperature. Electrons are transmitted from the occupied states in the left electrode to the unoccupied states in the right electrode. The left and right boundaries of the insulating barrier are indicated by z_1 and z_2 , respectively^[17].

We assume that the system has translational symmetry in the transverse (x and y) direction and therefore the wave vector parallel to the barrier surface $k_{\parallel} = (k_x, k_y)$ is conserved during the tunneling. We also assume that the temperature is zero. The number of electrons incident from the left electrode per unit time with wave vector k_{\parallel} is given by

$$N(k_{\parallel}) = 2 \times \frac{1}{2} \int_0^{eV} dE v_z(E, k_{\parallel}) \frac{1}{\pi \hbar v_z(E, k_{\parallel})} = 2 \frac{eV}{h} \quad (3.1)$$

where $v_z(k_{\parallel})$ is the velocity along the z direction and $1/\pi \hbar v_z(k_{\parallel})$ is the corresponding 1D density of states for the one spin channel. The factor 2 in equation (3.1) is due to the spin-degeneracy of the energy bands in the nonmagnetic electrode. Note that the number of incident electrons is independent of the wave vector k_{\parallel} . The tunnel current density is obtained by summing up the number of electrons tunneling through the barrier:

$$I = e \int \frac{dk_{\parallel}^2}{(2\pi)^2} N(k_{\parallel}) T(k_{\parallel}) = 2 \frac{e^2 V}{h} \int \frac{dk_{\parallel}^2}{(2\pi)^2} T(k_{\parallel}) \quad (3.2)$$

where $T(k_{\parallel})$ is the transmission probability defined as the ratio between the probability current densities of incident and transmitting waves. Here we assume the bias voltage V is so small that we can neglect the energy dependence of the transmission probability. The differential conductance per unit

area is written in terms of the transmission probability as

$$G \equiv \frac{dI}{dV} = 2 \frac{e^2}{h} \int \frac{dk_{\parallel}^2}{(2\pi)^2} T(k_{\parallel}) \quad (3.3)$$

The transmission probability $T(k_{\parallel})$ is obtained by solving the 1D Schrodinger equation:

$$-\frac{\hbar^2}{2m} \frac{\partial^2}{\partial z^2} \psi(z) = \left(E - V(z) - \frac{\hbar^2}{2m} k_{\parallel}^2 \right) \psi(z) \quad (3.4)$$

in the geometry shown in 3.1. The general solutions of equation (3.4) in the left (L) electrode, barrier (B), and right (R) electrode are, respectively, of the forms

$$\begin{aligned} \psi_L(z) &= a_L e^{ik_L z} + b_L e^{-ik_L z} && \text{for } z \leq z_1 \\ \psi_B(z) &= a_B e^{i\kappa z} + b_B e^{-i\kappa z} && \text{for } z_1 < z \leq z_2 \\ \psi_R(z) &= a_R e^{ik_R z} + b_R e^{-ik_R z} && \text{for } z > z_2 \end{aligned} \quad (3.5)$$

where the z components of the wave numbers are defined as

$$\begin{aligned} k_L &= \sqrt{(2m/\hbar^2)(E - V_L) - k_{\parallel}^2} \\ \kappa &= \sqrt{k_{\parallel}^2 - (2m/\hbar^2)(E - V_B)} \\ k_R &= \sqrt{(2m/\hbar^2)(E - V_R) - k_{\parallel}^2} \end{aligned} \quad (3.6)$$

The scattering wave in the whole system is given by the combination of eigen functions in equation (3.5). The coefficients a_L, b_L, a_B, b_B, a_R and b_R are determined by matching the slope and value of the wave function across the interface^[27]. The matching conditions at $z = z_1$ are conveniently described as a 2×2 matrix R_1 operating on the $2D$ vectors as

$$\begin{pmatrix} a_L \\ b_L \end{pmatrix} = R_1 \begin{pmatrix} a_B \\ b_B \end{pmatrix} \quad (3.7)$$

where

$$R_1 = \frac{1}{2k_L} \begin{pmatrix} (k_L - i\kappa)e^{(-ik_L + \kappa)z_1} & (k_L + i\kappa)e^{(-ik_L - \kappa)z_1} \\ (k_L + i\kappa)e^{(ik_L + \kappa)z_1} & (k_L - i\kappa)e^{(ik_L - \kappa)z_1} \end{pmatrix} \quad (3.8)$$

In the same manner, the matching conditions at $z = z_2$ are written as

$$\begin{pmatrix} a_B \\ b_B \end{pmatrix} = R_2 \begin{pmatrix} a_R \\ b_R \end{pmatrix} \quad (3.9)$$

where

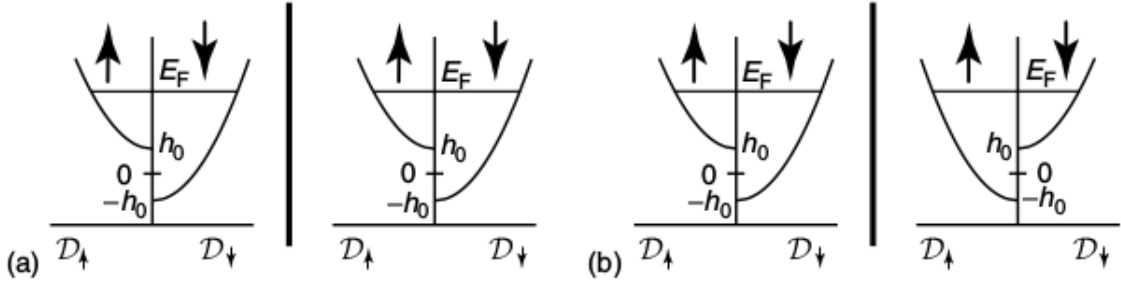


Figure 3.2: Densities of states for spin-up ($D \uparrow$) and spin-down ($D \downarrow$) electrons in the F alignment (a) and those in the A alignment (b)^[17]

$$R_2 = \frac{i}{2\kappa} \begin{pmatrix} (k_R - i\kappa)e^{(ik_R - \kappa)z_2} & -(k_R + i\kappa)e^{-(ik_R + \kappa)z_2} \\ -(k_R + i\kappa)e^{(ik_R + \kappa)z_2} & (k_R - i\kappa)e^{-(ik_R - \kappa)z_2} \end{pmatrix} \quad (3.10)$$

Since the quantity that we wish to compute is the transmission probability for the electron incident from the left electrode, only a transmitted wave exists in the right electrode and $b_R = 0$. The relation between the coefficients a_L , b_L and a_R is

$$\begin{pmatrix} a_L \\ b_L \end{pmatrix} = R_1 R_2 \begin{pmatrix} a_R \\ 0 \end{pmatrix} \quad (3.11)$$

Thus, the transmission probability is

$$T(k_{||}) = \frac{|a_R|^2 k_R}{|a_L|^2 k_L} = \frac{k_R}{k_L} \frac{1}{|(R_1 R_2)_{11}|^2} \quad (3.12)$$

$d = z_2 - z_1$ is the thickness or the length of the barrier.

Next, let us consider the magnetic tunnel junctions, where the conductance is spin-dependent. In the magnetic electrodes, spin-up and spin-down electrons feel the different exchange potentials h_0 and $-h_0$, respectively. The matching condition depends on the relative angle between the magnetization vectors of left and right electrodes. For simplicity, we consider two types of alignments of magnetization vectors, parallel (F, because it is similar to ferromagnetic) and anti-parallel (A) alignments, as shown in Figure 3.2.

The spin quantization axis is taken to be parallel to the magnetization vector in the left electrode. For the F alignment, where the magnetization vectors are parallel, we have two tunneling processes: electrons incident from the left majority (minority) spin band tunnel to the right majority (minority) spin band. Potential diagrams for these two tunneling processes are shown in Figure 3.3(a) and (b), respectively. The wave numbers of electrons in the majority and minority spin bands are

$$k_M = \sqrt{(2m/\hbar^2)(E - h_0) - k_{||}^2}, \quad k_m = \sqrt{(2m/\hbar^2)(E + h_0) - k_{||}^2} \quad (3.13)$$

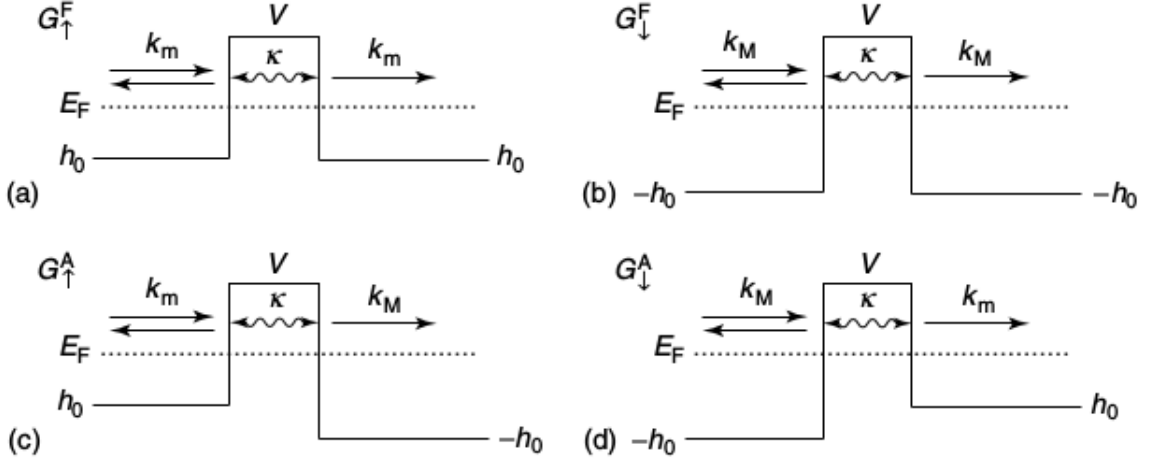


Figure 3.3: Geometries of the potentials for spin-up and spin-down electrons in the F alignment are shown in panels a) and (b), and those in the A alignment are shown in (c) and (d), respectively

The conductance for spin-up (spin-down) electrons is obtained from equation (3.3) and (3.12) by setting $k_L = k_R = k_M(k_m)$, where $k_M(k_m)$ is the wave number for the electrons in the majority (minority) spin band. The total conductance for the F alignment is: $G^P = G_{\uparrow}^P + G_{\downarrow}^P$. In contrast, for the A alignment where the magnetization vectors are antiparallel, electrons incident from the left majority (minority) spin band tunnel to the right minority (majority) spin band. The potential diagrams for spin-up and spin-down electrons are depicted in Figure 3.3(c) and (d), respectively.

The conductance for the A alignment, G^A is given from equation (3.3) and (3.12) by setting $k_L = k_M(k_m)$ and $k_R = k_m(k_M)$, where $k_M(k_m)$ is the wave number for the electrons in the majority (minority) spin band

Using G^F and G^A , the TMR is expressed as¹⁷

$$TMR = \frac{G^F - G^A}{G^A} \quad (3.14)$$

The tunneling conductances, G^F (both G_{\uparrow}^F and G_{\downarrow}^F) and G^A and TMR for a nanowire (or nanopillar) are different from that of the similar parameters for the current flowing through MTJs which consists of planar layers (with almost infinitely wide cross-sectional area compared to the de-Broglie wavelength of the electron). The conductances and TMR for a nanowire vary a lot due to changes in wire dimensions or barrier length or barrier potential or when an array of wires are considered.

3.2 Variation of transmission probability with the thickness d of the insulating barrier

The density of states is slightly shifted up by $h_0 = 0.2eV$ for minority spin electrons and shifted down by the same $h_0 = 0.2eV$ for majority spin electrons from the zero energy level. In this case, downspin

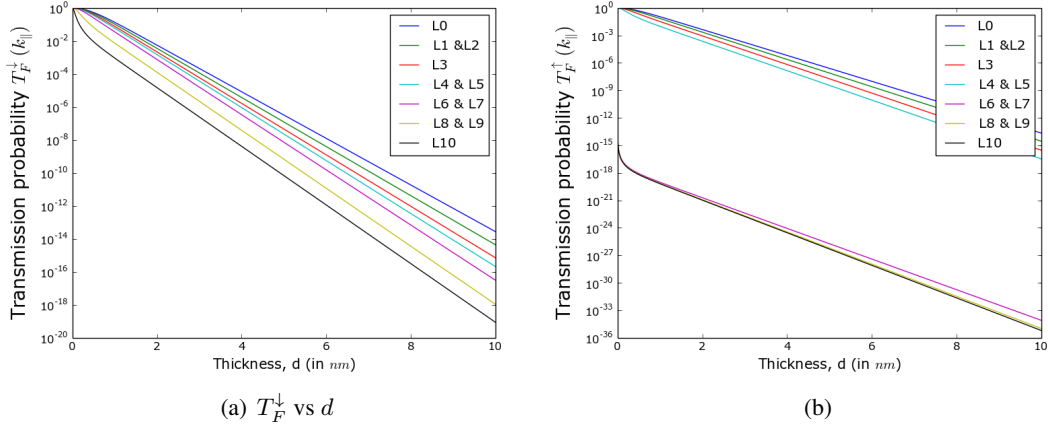


Figure 3.4: Transmission probability, T_F vs barrier length d for nanowire ($V_B = 2.2V$)

\downarrow is considered as the majority spin. That means, the majority spin electrons has more number of states. Equation (3.12), describes the dependence of these allowed states to the transmission probability for tunneling through the barrier. There are more number of majority spin electrons available for conduction. Depending on the alignment ($F \downarrow$ or $F \uparrow$ or A), the transmission probability is different. The length of the insulating MgO barrier d too changes the transmision probability of the electrons of different spins.

3.2.1 Parallel alignment

The transmission probability for electrons in F alignment, T_F^\downarrow or T_F^\uparrow is plotted for every eigen energy mode or state as d is varied in fig 3.4. For all the states, the probability of tunneling decreases drastically as the barrier length increases. This is because, during quantum tunneling through MgO barrier, the probability amplitude exponentially decays as a function of distance, thus reducing the probability to reach the other side. Lower energy states have more transmission probability. This is because, for a given energy of an electron, the confinement energy (E_{2D}) is lower for lower energy states by definition and so, the remaining energy for traversing through the wire is more for lower energy states. T_F^\uparrow for higher energy modes are much lower than the lower modes because the electrons from those modes are not available as those higher modes have energies more than the Fermi energy, $E_F = 0.8eV$. Now, this Fermi energy translates to $E_F + h_0 = 1.0eV$ for majority electrons and $E_F - h_0 = 0.6eV$ for minority electrons. For the $10nm$ wire, first six modes have energy lower than $0.6eV$, so the minority electrons in modes above that energy are no more available, resulting in very less T_F^\uparrow .

3.2.2 Anti-parallel alignment

The behaviour of the transmission probability for anti-parallel alignment is similar to that of the parallel alignment (fig 3.5). T_A is lower than T_F^\downarrow (majority) and greater than T_F^\uparrow (minority), except when the barrier is very thin, i.e., when $\kappa d \ll 1$. At such short barriers, a lot of electrons get reflected by the spin band barriers of the right substrate and get transmitted back to the initial (left) substrate traversing again through the barrier in (A) alignment. So, eventually, the T_A is the lowest only for such thin barriers.

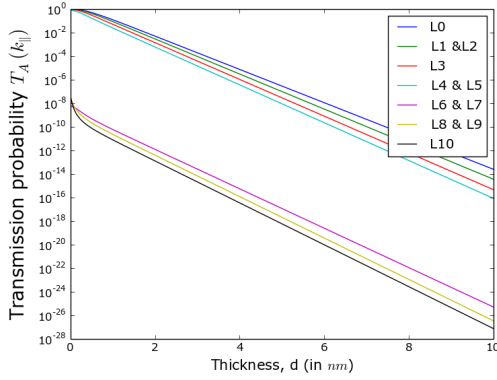


Figure 3.5: Transmission probability, T_A vs barrier length d ($V_B = 2.2V$)

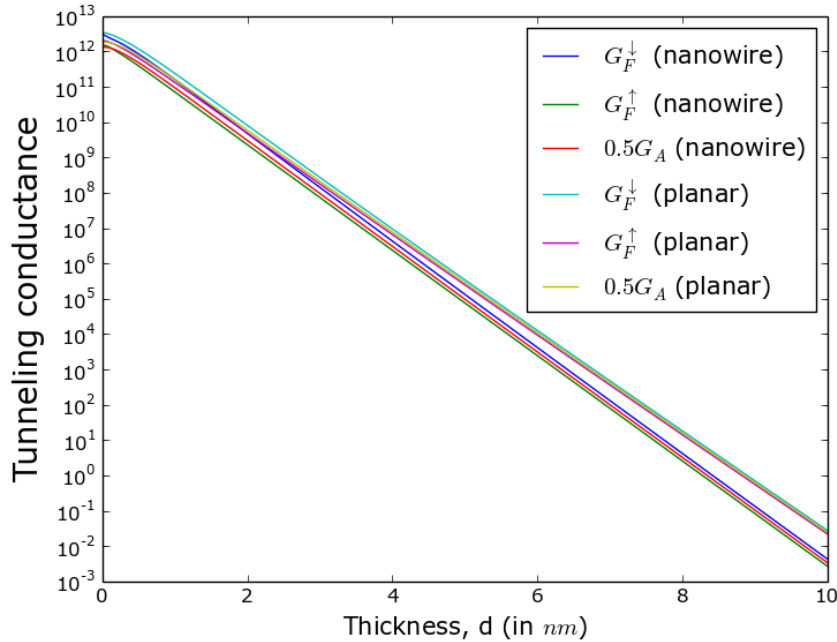


Figure 3.6: Tunneling conductance per unit area vs barrier length d ($V_B = 2.2V$)

3.3 Variation of tunneling conductance with the thickness d of the insulating barrier

The tunneling conductance, given by (3.3) depends on the transmission probability of electron tunneling through an insulating barrier, MgO. It is integrated over all the available energy states of the conduction electrons. It is studied for magnetic tunnel junction which has a planar barrier (relatively infinite cross-sectional area) and for barrier in nanowire (or nanopillar) tunnel junction (cross-sectional area in nano regime). The expression (3.3) becomes a summation over all the available states for nanowire case.

The variation of the tunneling conductance for parallel alignment and anti-parallel alignment as the length d of the insulating barrier was changed is shown in fig 3.6. Transmission probability decreases drastically with increasing barrier length, fig 3.4 and 3.5. Tunneling conductance is just the summation

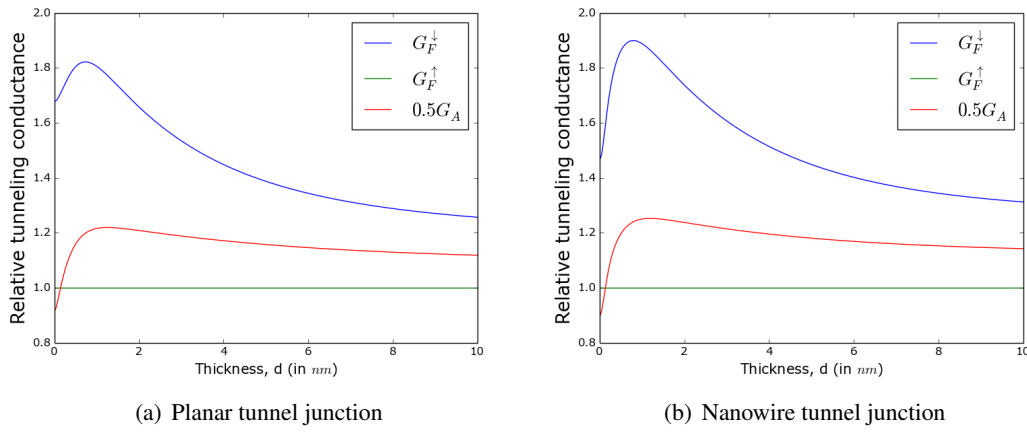


Figure 3.7: Relative tunneling conductance vs barrier thickness ($V_B = 2.2V$)

(or integration) of the probabilities over all the states. So, its behaviour is expected to be similar and it actually is similar. But, conductance is more for planar tunnel junction, because it allows a lot of electrons to flow through.

3.3.1 Planar magnetic tunnel junction

Relative tunneling conductance (compared to G_F^\uparrow (minority)) for planar tunnel junction (fig 3.7(a)), reaches a maximum and drops down because, majority electrons scatter more due to the presence of lot of them and eventually G_F^\downarrow and G_A starts dying down. When the barriers are very thin, the electrons are able to reflect back to the left substrate itself in the (A) alignment, because of imbalance in the number of states available in the substrates on both sides. So, $G_A < G_F^\uparrow$ for very thin barriers.

3.3.2 Nanowire magnetic tunnel junction

Relative tunneling conductance for nanowire (or nanopillar) tunnel junction also reaches a maximum and drops down due to similar reasons as that of the planar case (3.7(b)).

3.4 Variation of TMR with the thickness d of the insulating barrier

Tunneling magneto resistance (TMR) given by (3.14) depends on the relative difference between the conductances in the parallel (F) alignment and in the anti-parallel (A) alignment for a given energy. These conductances depend on the length of the barrier, so TMR too depends on the length of the insulating barrier. As mentioned earlier, electrons with energy below Fermi energy only are available in the metal substrate. Now, this Fermi energy translates to $E_F + h_0 = 1.0\text{eV}$ for majority electrons and $E_F - h_0 = 0.6\text{eV}$ for minority electrons as described earlier. This difference causes differences in the tunneling conductances of electrons of different spins. From (3.14), this relative difference is known as TMR.

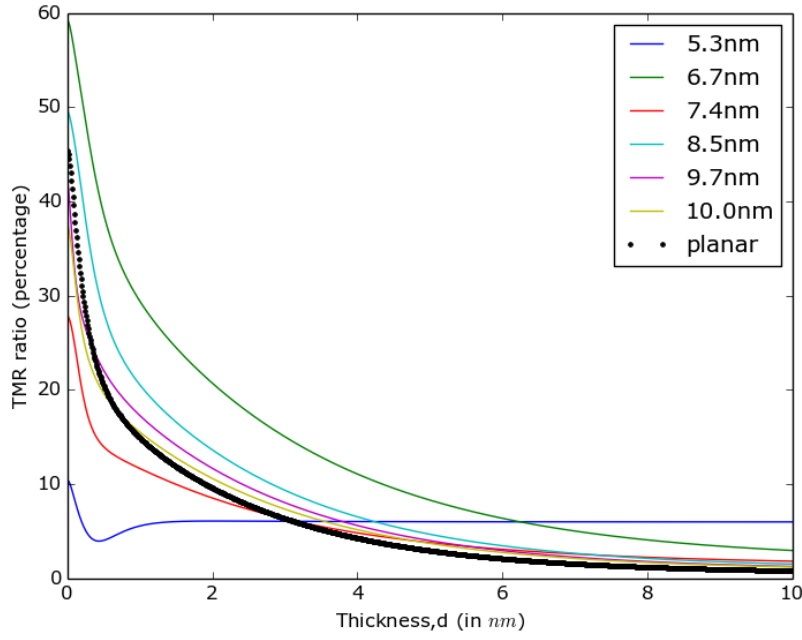


Figure 3.8: TMR vs barrier thickness, d for different wire dimensions $V_B = 2.2V$

Actually, for a given energy of electrons and size of the nanowire, there are only a certain number (finite) of states that are allowed, unlike the planar tunnel junction, where a density of states is considered, because continuous set of (infinite) states are allowed in the planar case. So, here, the nanowire dimensions considered are in such a way that, there is one additional non-degenerate energy mode that gets added as the dimensions are increased. For example, wire with dimensions 5.3nm has two energy non-degenerate modes below E_F , the Fermi energy or the total energy. Similarly, the wire with dimensions 6.7nm has three non-degenerate energy modes below E_F , and the wire with dimensions 7.4nm has four non-degenerate energy modes below E_F and so on. Finally, the case with the planar junction is also considered, which apparently has infinite states below E_F .

For all dimensions of the nanowire (even for the planar junction case), TMR decreases as the barrier thickness increases (3.8) because of reduction of the effect of spin filtering for thicker barriers. Yet, for different barrier thicknesses, this effect reduces differently. It shows a damped oscillating behaviour (3.8). That is, the wire with dimensions 5.3nm has very low TMR, while the wire with dimension 6.7nm has very high TMR. Again, the wire with dimension 7.4nm has lower TMR than the planar case, but more than the 5.3nm wire and so on, until it reaches the planar case. But, when the insulating barrier thickness d considered is as large as $8 - 10\text{nm}$, then this oscillating behaviour is not seen, rather wires with smaller dimensions have more TMR than the wires with larger dimensions (3.8). Moreover, the 5.3nm wire has TMR value which is almost constant, except for a dip when d is very small.

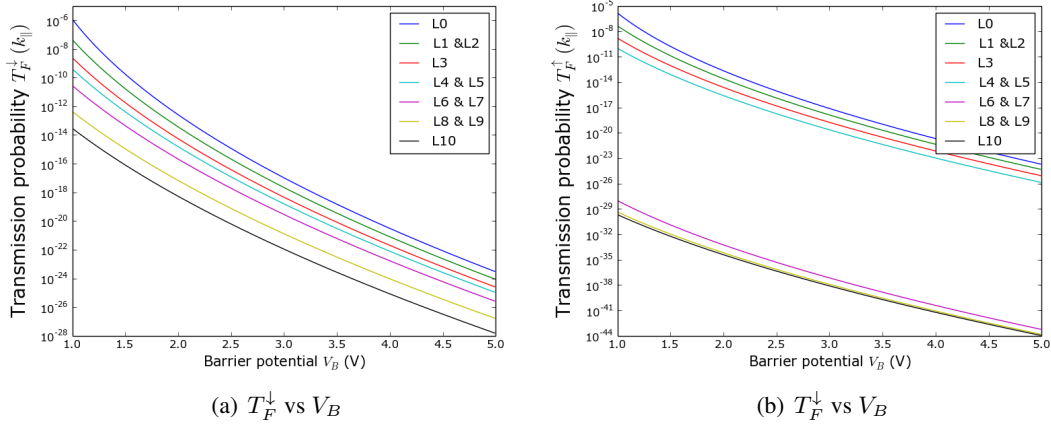


Figure 3.9: Transmission probability, T_F vs barrier potential V_B ($d = 10\text{nm}$)

3.5 Behaviour of transmission probability with the barrier potential V_B

Depending on the alignment ($F \downarrow$ or $F \uparrow$ or A), the transmission probability is different. When a different material is used as an insulating barrier like Al_2O_3 , instead of MgO and with different crystal compositions or configurations, the barrier potential V_B changes. This affects κ (3.6), which in turn changes the probability of electrons tunneling through the barrier for different alignments of the magnetization vectors. It actually changes the probability of electrons that gets reflected and transmitted at both the metal-insulator interfaces, thus modifying a lot of parameters that depends on these probabilities. The density of states is slightly shifted up by $h_0 = 0.2\text{eV}$ for minority spin electrons and shifted down by the same $h_0 = 0.2\text{eV}$ for majority spin electrons from the zero energy level. In this case, downspin \downarrow is considered as the majority spin. That means, the majority spin electrons has more number of states. Equation (3.12), describes the dependence of these allowed states to the transmission probability for tunneling through the barrier. There are more number of majority spin electrons available for conduction. Depending on the alignment ($F \downarrow$ or $F \uparrow$ or A), the transmission probability is different. The length of the insulating MgO barrier d too changes the transmision probability of the electrons of different spins

3.5.1 Parallel alignment

The transmission probability for electrons in F alignment, T_F^\downarrow or T_F^\uparrow is plotted for every eigen energy mode or state as V_B is varied (keeping barrier thickness $d = 10\text{nm}$ constant), in fig 3.9. For all the states, the probability of tunneling decreases drastically as the barrier potential (height) increases. This is because, during quantum tunneling through MgO or Al_2O_3 barrier, the probability amplitude exponentially decays as a function of distance and κ , thus reducing the probability to reach the other side. Lower energy states have more transmission probability. This is because, for a given energy of an electron, the confinement energy (E_{2D}) is lower for lower energy states by definition and so, the remaining energy used for traversing through the wire and tunneling through the barrier is more for lower energy states. As explained in an earlier section, the minority electrons are not much available at high energy

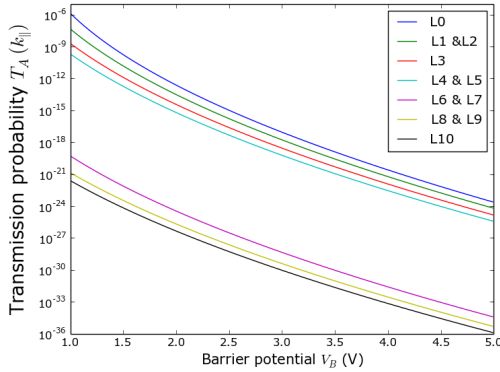


Figure 3.10: Transmission probability, T_A vs barrier height V_B ($d = 10\text{nm}$)

modes, therefore T_F^\uparrow is comparatively very low for those modes.

3.5.2 Anti-parallel alignment

The behaviour of the transmission probability for anti-parallel alignment is similar to that of the parallel alignment (fig 3.10). T_A is lower than T_F^\downarrow (majority) and greater than T_F^\uparrow (minority), except when the barrier potential is very small, i.e., when $\kappa d \ll 1$. At such short barriers, a lot of electrons get reflected by the spin band barriers of the right substrate and get transmitted back to the initial (left) substrate traversing again through the barrier. This transition of the probabilities happens at a particular value of V_B for different energy levels. Higher the level, lower the transition barrier potential, because (3.6) suggests κ to be the sum of V_B and $k_{\parallel}^2 \propto E_{2D}$.

3.6 Behaviour of tunneling conductance with the barrier potential V_B

The tunneling conductance, given by (3.3) depends on the transmission probability of electron tunneling through an insulating barrier. It is integrated over all the available energy states of the conduction electrons. It is again studied for magnetic tunnel junction which has a planar barrier (relatively infinite cross-sectional area) and for barrier in nanowire tunnel junction (cross-sectional area in nano regime) for varying barrier potentials. The expression (3.3) becomes a summation over all the available states for nanowire case.

The variation of the tunneling conductance for parallel alignment and anti-parallel alignment as the potential (or height) of the insulating barrier V_B was changed (keeping barrier thickness $d = 10\text{nm}$ constant) is shown in fig ???. Transmission probability decreases drastically with increasing V_B , figs 3.9 and 3.10. Tunneling conductance is just the summation (or integration) of the probabilities over all the states. So, its behaviour is similar. But, conductance is more for planar tunnel junction, because it allows a lot of electrons.

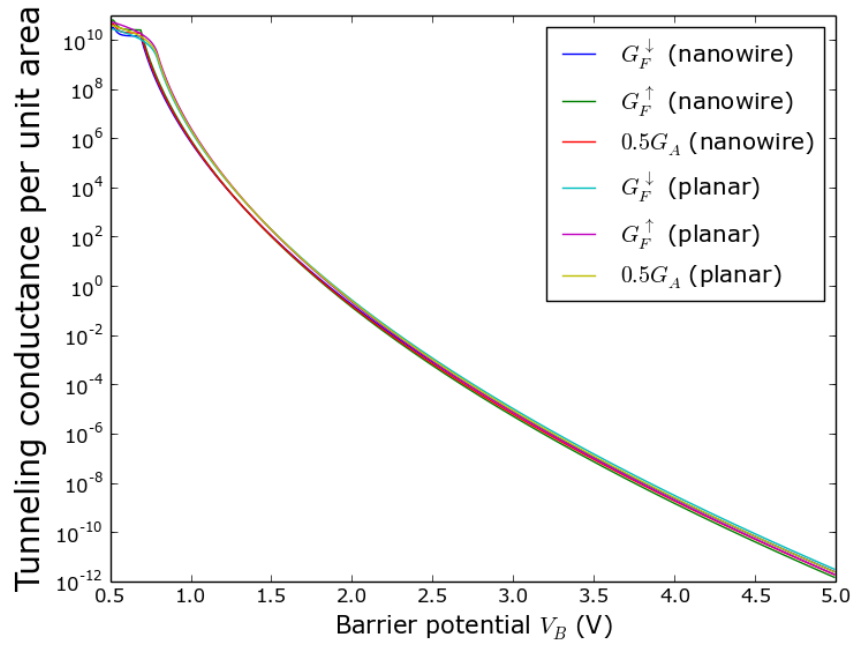


Figure 3.11: Tunneling conductance per unit area vs barrier potential V_B ($d = 10\text{nm}$)

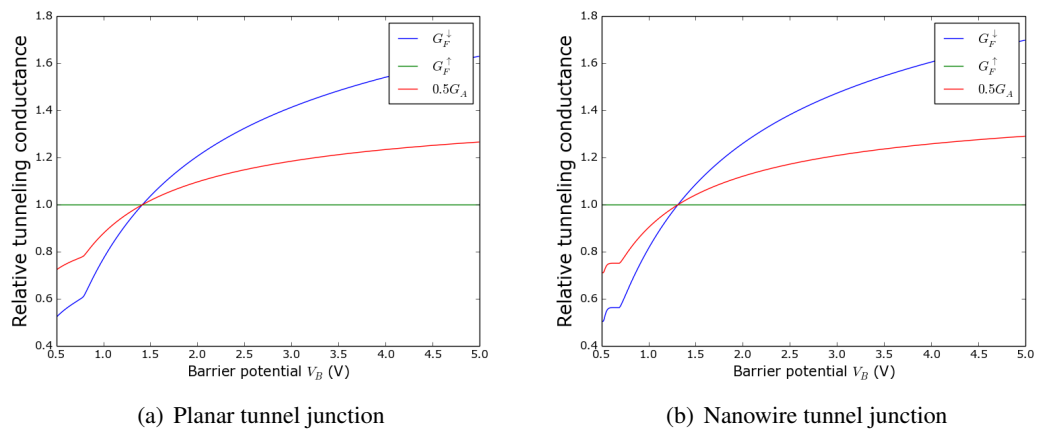


Figure 3.12: Relative tunneling conductance vs barrier potential V_B ($d = 10\text{nm}$)

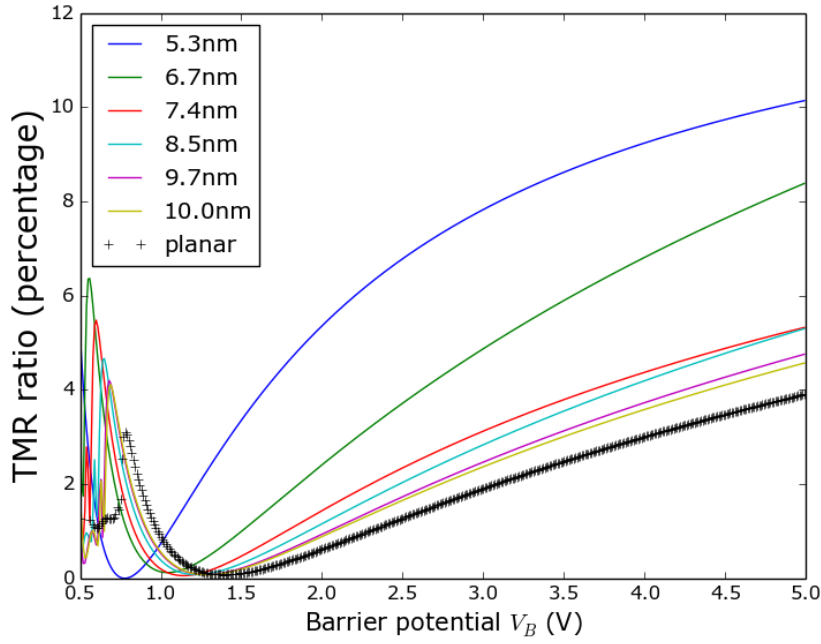


Figure 3.13: TMR vs barrier height V_B for different wire dimensions ($d = 10\text{nm}$)

3.6.1 Planar magnetic tunnel junction

Unlike the dependence on barrier thickness d , dependence on barrier potential V_B affects the probability of reflection and transmission at both the metal-insulator interfaces too (fig ??(a)). The combined effect of the change in the probabilities and the change in the amount of scattering that happens for a given energy inside the insulating barrier, results in a steady increase in the tunneling conductances (G_F^\downarrow and G_A) relative to G_F^\uparrow . The change in comparative behaviour of the transmission probabilities for different alignments described in the earlier section is clearly shown in 3.12, where at around $V_B \approx 1.4\text{V}$, $G_F^\downarrow = G_F^\uparrow = G_A$.

3.6.2 Nanowire magnetic tunnel junction

Relative tunneling conductance for nanowire tunnel junction also steadily increases due to similar reasons as that of the planar case (fig 3.7(b)). Only the cross-sectional area is in nanometer regime.

3.7 Behaviour of TMR with the barrier potential V_B

The tunnelling conductances depend on the barrier potential V_B , so TMR too depends on V_B . Similar to the case where the thickness of the barrier was varied, here too, the nanowire dimensions are considered are in such a way that, there is one additional non-degenerate energy level that gets added (below $E_F = 0.8\text{eV}$) as the dimensions are increased. Finally, the case with the planar junction is also considered, which apparently has infinite states below $E_F = 0.8\text{eV}$.

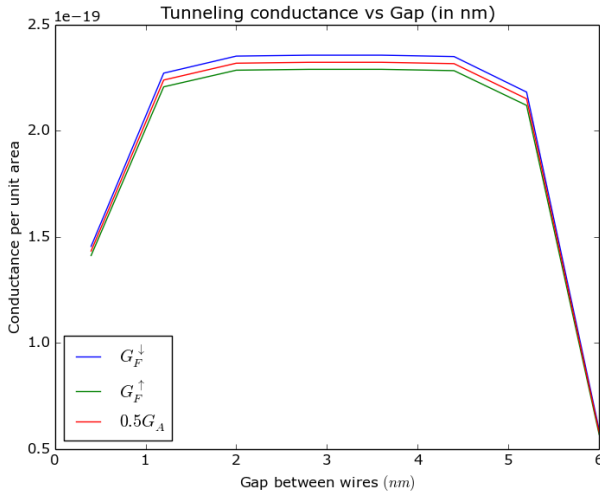


Figure 3.14: Tunneling conductances vs gap between wires

For all dimensions of the nanowire (even for the planar junction case), TMR decreases as the barrier potential V_B increases for lower potentials (above Fermi energy) (fig 3.13). This is because of reduction of the effect of spin filtering for increasing barrier potentials. But, for all wire dimensions, TMR then reaches a minimum, which is zero and starts increasing for higher values of V_B . That's when $G_F^\downarrow = G_F^\uparrow = G_A$. Now, this is because, as V_B increases, more reflections happen at both the metal-insulator interfaces, causing a steady increase in the values of TMR for nanowire tunnel junctions of various dimensions and for the planar MTJ too. The value of V_B for each wire (of certain dimensions) at which the TMR reaches minimum, increases from about 0.7V to about 1.4V for wires with greater dimensions (side of the cross-sectional area) i.e. from 5.3nm to 10.0nm to planar (fig 3.13). This is because the effect of reflections starts dominating in effecting TMR early, i.e., even at lower values of V_B , for wires with lesser number of allowed energy levels, meaning wires with smaller dimensions. Now, interestingly, when $V_B < E_F$, the electrons start crossing over the barrier, because, electrons in modes of higher energy have more energy than the barrier. This causes oscillating behaviour of TMR because those modes have discrete energies.

3.8 Tunneling parameters for an array of 4 quantum wires

Though single wire is easy for modelling, in practice, only an array of wires is often used. The spin-dependent tunneling conductances and TMR are studied for electrons flowing through 4 quantum wires of dimension 2nm each placed apart on a substrate, as the gap between the wires are changed.

3.8.1 Tunneling conductance vs gap between wires

Tunneling conductance stays constant when the gap between the wires is between about 2nm to about 4.5nm, i.e. when the wires are not very close to each other nor when they are very close to the edges (fig 3.14). When the gap between the wires is lower than this range, the system behaves as if there is a single larger wire in the centre, because of lateral quantum tunneling between the wires. But, more lateral

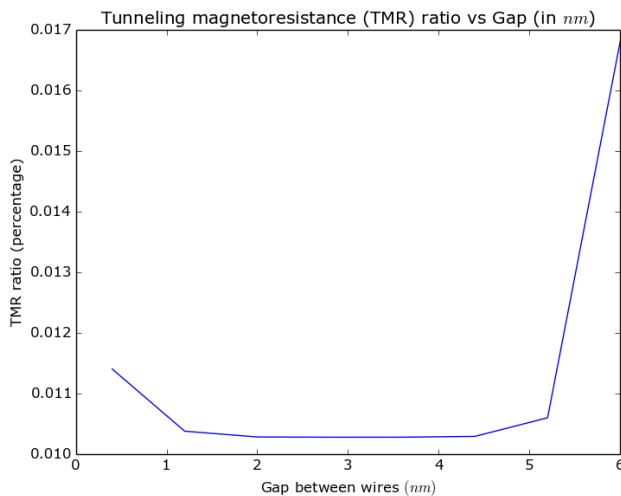


Figure 3.15: TMR vs gap between wires

reflections happen causing some electrons to leak into the substrate, thus reducing the conductance. Also when the gap between the wires are so much that it is about half the wire size distance from the boundaries (of the lattice), the conductances decrease because the electrons get reflected from the infinite lattice boundaries and need more energy to stay confined and flow through the wires close to the boundaries.

3.8.2 Tunneling Magneto Resistance (TMR) vs gap between wires

The TMR, in fact reflects the behaviour of the tunneling conductance. TMR increases for both the extreme cases, i.e. when the wires are very close apart and when they are very close to the edges (fig 3.15). This happens because, although the difference between G_F and G_A remains almost same, their actual value reduces drastically, in turn increasing TMR at those extreme cases (as $TMR \propto \frac{1}{G_A}$).

CHAPTER 4

Spin Transfer Torque

4.1 Theory and applications of Spin Transfer Torque

Spin-transfer torque is an effect in which the orientation of a magnetic layer in a magnetic tunnel junction or spin valve can be modified using a spin-polarized current.

Charge carriers (such as electrons) have a property known as spin which is a small quantity of angular momentum intrinsic to the carrier. An electrical current is generally unpolarized (consisting of 50 spin-up and 50 spin-down electrons); a spin polarized current is one with more electrons of either spin. By passing a current through a thick magnetic layer (usually called the "fixed layer"), one can produce a spin-polarized current. If this spin-polarized current is directed into a second, thinner magnetic layer (the "free layer"), angular momentum can be transferred to this layer, changing its orientation. This can be used to excite oscillations or even flip the orientation of the magnet. The effects are usually only seen in nanometer scale devices. Spin-transfer torque can be used to flip the active elements in magnetic random-access memory. Spin- transfer torque magnetic random-access memory (STT-RAM or STT-MRAM) has the advantages of lower power consumption and better scalability over conventional magnetoresistive random-access memory (MRAM) which uses magnetic fields to flip the active elements.

4.1.1 Metal-Ferromagnetic junction

When a current of polarized electrons enters a ferromagnet, there is generally a transfer of angular momentum between the propagating electrons and the magnetization of the film. This concept of "spin transfer" was proposed independently by Slonczewski^[29] and Berger^[30] in 1996. Experiments soon followed where anomalies in the current-voltage characteristics of magnetic heterostructures were interpreted as evidence for spin transfer^[31]. Unambiguous confirmation came when the phenomenon of giant magnetoresistance^[32] was used to detect magnetization reversal in ferromagnetic multilayers with large current densities flowing perpendicular to the plane of the layers^{[33]–[35]}. Subsequently, spin transfer has been implicated to explain the observation of spin precession for high-energy, spin-polarized electrons that traverse a magnetic thin film^[36] and enhanced Gilbert damping in magnetic multilayers compared to one-component magnetic films^[37]. More experiments may be expected in the future because spin transfer is expected to play an important role in the nascent field of "spin electronics"^[38].

4.1.2 Particle Transport

The wave vector for an electron with state index i (Energy level) and spin index σ (up or down) is $|\psi_{i\sigma}; E_i, \pm \frac{\hbar}{2}\rangle$. For a single particle, the wave vector is a superposition of different states.

$$|\psi\rangle = \sum_{i\sigma} |\psi_{i\sigma}\rangle \quad (4.1)$$

We define the wave function as $\psi_{i\sigma}(\mathbf{r}) \equiv \langle \mathbf{r} | \psi_{i\sigma}; E_i, \pm \frac{\hbar}{2} \rangle$.

The number density is

$$n(\mathbf{r}) = \sum_{i\sigma} \psi_{i\sigma}^*(\mathbf{r}) \psi_{i\sigma}(\mathbf{r}) \quad (4.2)$$

The number current density ¹ is

$$\mathbf{j}(\mathbf{r}) = \Re \left[\sum_{i\sigma} \psi_{i\sigma}^*(\mathbf{r}) \hat{\mathbf{v}} \psi_{i\sigma}(\mathbf{r}) \right], \quad (4.3)$$

where $\hat{\mathbf{v}} = -(i\hbar/m)\nabla$ is the velocity operator.

We are interested in steady state solution where n is independent of time. Not far from equilibrium, the current takes the phenomenological form (drift and diffusion)

$$\mathbf{j} = (\sigma/e)\mathbf{E} - D\nabla\delta n, \quad (4.4)$$

where $\delta n = n - n_{eq}$ and D is the diffusion constant.

4.1.3 Spin Transport

The Spin Density is defined as an expectation over the Pauli matrices as

$$\begin{aligned} \mathbf{m}(\mathbf{r}) &= \langle \mathbf{s} \rangle \\ &= \sum_{i\sigma\sigma'} \psi_{i\sigma}^*(\mathbf{r}) s_{\sigma\sigma'} \psi_{i\sigma'}(\mathbf{r}) \end{aligned}$$

$\mathbf{s} = (\hbar/2)\sigma$ where $\sigma = \sigma_x \hat{\mathbf{x}} + \sigma_y \hat{\mathbf{y}} + \sigma_z \hat{\mathbf{z}}$.

$$\begin{aligned} \sigma_x &= \begin{pmatrix} 0 & 1 \\ 1 & 0 \end{pmatrix} \\ \sigma_y &= \begin{pmatrix} 0 & -i \\ i & 0 \end{pmatrix} \\ \sigma_z &= \begin{pmatrix} 1 & 0 \\ 0 & -1 \end{pmatrix} \end{aligned}$$

$\langle \mathbf{s} \cdot \hat{\mathbf{r}} \rangle$ gives the expectation of spin when measured along $\hat{\mathbf{r}}$.

¹Satisfies the continuity equation $\frac{\partial n(\mathbf{r})}{\partial t} + \nabla \cdot \mathbf{j}(\mathbf{r}) = 0$ for a conserved quantity. In this article, we derive $\mathbf{j}(\mathbf{r})$ by using the Schrodinger equation for a free particle in an electric field and not in a magnetic field, $\left(i\hbar \frac{\partial \psi}{\partial t} = \left[\frac{-\hbar^2}{2m} \nabla^2 + V \right] \psi \right)$.

We define the Spin current density by analogy to particle transport as

$$\mathbf{Q}(\mathbf{r}) = \Re \left[\sum_{i\sigma\sigma'} \psi_{i\sigma}^*(\mathbf{r}) s_{\sigma\sigma'} \otimes \hat{\mathbf{v}} \psi_{i\sigma'}(\mathbf{r}) \right] \quad (4.5)$$

Unlike particle transport, we consider spin accumulation and generation in the continuity equation². We get

$$\nabla \cdot \mathbf{Q} + \frac{\partial \mathbf{m}}{\partial t} = -\frac{\delta \mathbf{m}}{\tau_{\uparrow\downarrow}} + n_{ext} \quad (4.6)$$

where \mathbf{Q} is a tensor with Q_{ik} as current along spin axis i flowing spatially through axis k .

$\nabla \cdot \mathbf{Q} = \partial_k Q_{ik}$ where $\delta \mathbf{m} = (|\mathbf{m}| - m_{eq})\hat{\mathbf{m}}$ is spin accumulation due to transfer of angular momentum between spin current and the lattice due to spin-flip. The relaxation time $\tau_{\uparrow\downarrow}$ changes with magnitude of local spin density but not direction.

The Landau-Lifshitz-Gilbert torque density gives $n_{ext} = -(g\mu_B/\hbar)\mathbf{m} \times \mathbf{B}_{eff} + \alpha \hat{\mathbf{m}} \times \dot{\mathbf{m}}$ where the first term is spin torque due to applied magnetic field and the second term is phenomenological damping. In this article we study the spin transfer torque density $\mathbf{n}_{stt} = -\nabla \cdot \mathbf{Q}$.

Phenomenologically the spin current is driven by drift and diffusion,

$$Q_{ik} = \bar{\sigma}_i E_k - \bar{\Lambda}_i \partial_k \delta m_i \quad (4.7)$$

$\bar{\sigma} = (\sigma_{\uparrow} - \sigma_{\downarrow})\hat{\mathbf{m}}$ and $\bar{\Lambda}$ also proportional to the same rather than thirf rank tensors. \bar{D} is taken to be a scalar rather than a fourth rank tensor.

In a nonmagnet, $\sigma_{\uparrow} - \sigma_{\downarrow}$. Hence, spin current occurs only if there is a gradient in spin accumulation. But, it is not so for a ferromagnet. Also the phenomenological transport equations are not valid if the direction of ferromagnetic magnetization is not uniform. Corrections are necessary when the magnetization rotates continuously in space like inside a domain wall.

We alter the phenomenological equation 4.4 by considering that spin accumulation also causes a flow in particle current to

$$j_i = (\sigma/e)E_i - D\partial_i \delta m_k$$

4.2 Free Electrons

Consider a free electron in a non-magnet travelling towards a ferromagnet with magnetization $M\hat{z}$. We choose a spin basis along the \hat{z} direction and define K_F^{\uparrow} and K_F^{\downarrow} as the fermi levels for majority and minority electrons for spin along \hat{z} .

²The choice of $\hat{H} = \left[\frac{-\hbar^2}{2m} \nabla^2 + V \right]$ we made to derive \mathbf{j} will force the RHS of (eqn) to be 0. The Hamiltonian has additional terms capturing n_{ext} and spin relaxation.

The transformation matrix³ between two spin basis at an angle θ, ϕ is given as

$$\begin{aligned}\mathbf{U} &= \exp\left(\frac{-i\sigma_z\phi}{2}\right) \cdot \exp\left(\frac{-i\sigma_y\phi}{2}\right) \\ &= \begin{pmatrix} e^{-i\frac{\phi}{2}} & 0 \\ 0 & e^{i\frac{\phi}{2}} \end{pmatrix} \cdot \begin{pmatrix} \cos\frac{\theta}{2} & -\sin\frac{\theta}{2} \\ \sin\frac{\theta}{2} & \cos\frac{\theta}{2} \end{pmatrix} \\ &= \begin{pmatrix} \cos\frac{\theta}{2}e^{-i\frac{\phi}{2}} & -\sin\frac{\theta}{2}e^{-i\frac{\phi}{2}} \\ \sin\frac{\theta}{2}e^{i\frac{\phi}{2}} & \cos\frac{\theta}{2}e^{i\frac{\phi}{2}} \end{pmatrix}\end{aligned}$$

Let the spin be polarized at an angle θ, ϕ in the non-magnet with spin $+\frac{1}{2}$ and travelling with wave vector $\mathbf{k} = (k_x, \mathbf{q})$ ⁴, and spatial variable as $\mathbf{r} = (x, \mathbf{R})$. It can be represented by $(|\uparrow'\rangle e^{ik_xx} e^{i\mathbf{q} \cdot \mathbf{R}})$. Then we have

$$\psi_{in} = \mathbf{U} |\uparrow'\rangle = \left[\cos \frac{\theta}{2} e^{-i\frac{\phi}{2}} |\uparrow\rangle + \sin \frac{\theta}{2} e^{i\frac{\phi}{2}} |\downarrow\rangle \right] e^{ik_xx} e^{i\mathbf{q} \cdot \mathbf{R}} \quad (4.8)$$

in the \hat{z} basis.

We set $\frac{\hbar^2 |\mathbf{k}^\sigma|^2}{2m} = E_F^\sigma$ as only conduction electrons are free.

We can split $\psi = \psi_{in} + \psi_{ref} + \psi_{tr}$ as ψ_\uparrow and ψ_\downarrow by suitable transformation of the wave vector. We assume that the transverse components $\mathbf{q} \cdot \mathbf{R}$ remain unaffected by the planar interface and hence drop $e^{i\mathbf{q} \cdot \mathbf{R}}$ as it is a constant phase in the wave function. The reflected wave travelling along $-\hat{x}$ but having the same fermi energy will have $\mathbf{k} = (-k_x, \mathbf{q})$. The transmitted waves have different fermi energy and we expect $\mathbf{k} = (k_x^\uparrow, \mathbf{q})$ for the spin up wave and similar expression for spin down.

$$\begin{aligned}\psi_\uparrow &= \cos \frac{\theta}{2} e^{-i\phi/2} |\uparrow\rangle \begin{cases} e^{ik_xx} + R_\uparrow e^{-ik_xx} & x < 0 \\ T_\uparrow e^{ik_x^\uparrow x} & x > 0 \end{cases} \\ \psi_\downarrow &= \sin \frac{\theta}{2} e^{i\phi/2} |\downarrow\rangle \begin{cases} e^{ik_xx} + R_\downarrow e^{-ik_xx} & x < 0 \\ T_\downarrow e^{ik_x^\downarrow x} & x > 0 \end{cases}\end{aligned} \quad (4.9)$$

ψ has to be continuous for the same electron. Also, continuity of $\frac{\partial\psi}{\partial x}$ should be applied, as there is only a finite Energy difference (follows from the Schrodinger's equation). Then, it results in 4 equations and 4 unknown transmission and reflection coefficients that could be solved.

$$T_\sigma(q) = \frac{2k_x(q)}{k_x(q) + k_x^\sigma(q)}, R_\sigma(q) = \frac{k_x(q) - k_x^\sigma(q)}{k_x(q) + k_x^\sigma(q)} \quad (4.10)$$

where $k_x^\sigma = \sqrt{(K_F^\sigma)^2 - q^2}$, ($\sigma \equiv \uparrow, \downarrow$). Note that if we have $q^2 > (K_F^\sigma)^2$ we have imaginary wave vectors, implying tunneling and not propagation as the amplitude decays. The expressions for the transverse spin current probabilities and transverse spin current density components are^[39]:

$$R^\sigma(q) = \frac{j_{ref\sigma}}{j_{in}} = R_\sigma R_\sigma^* = \left[\frac{k_x(q) - k_x^\sigma(q)}{k_x(q) + k_x^\sigma(q)} \right] \left[\frac{k_x(q) - k_x^\sigma(q)}{k_x(q) + k_x^\sigma(q)} \right]^*$$

³ $U_{\theta\hat{n}} = \exp\left(\frac{-i\mathbf{S} \cdot \hat{n}\theta}{\hbar}\right) = \mathbf{I} \cos \frac{\theta}{2} - i\hat{n} \cdot \boldsymbol{\sigma} \sin \frac{\theta}{2}$

⁴here $\mathbf{q} \equiv (k_y, k_z)$. Note that, unlike in earlier sections, in this section, electron is assumed to traverse along *+ve x-axis* direction

$$T^\sigma(q) = \frac{j_{tra\sigma}}{j_{in}} = \frac{\Re(k_x^\sigma(q))}{k_x(q)} T_\sigma T_\sigma^* = \frac{k_x^\sigma + (k_x^\sigma)^*}{2k_x} \left[\frac{2k_x(q)}{k_x(q) + k_x^\sigma(q)} \right] \left[\frac{2k_x(q)}{k_x(q) + k_x^\sigma(q)} \right]^*$$

$$|\hat{Q}_{xx} + \hat{Q}_{yx}| = \begin{cases} |R_\uparrow R_\downarrow^*| = \left| \left[\frac{k_x(q) - k_x^\uparrow(q)}{k_x(q) + k_x^\uparrow(q)} \right] \left[\frac{k_x(q) - k_x^\downarrow(q)}{k_x(q) + k_x^\downarrow(q)} \right]^* \right|, & x < 0 \\ \left| T_\uparrow T_\downarrow^* \Phi \right|_{x \rightarrow 100} = \left| \left[\frac{2k_x(q)}{k_x(q) + k_x^\uparrow(q)} \right] \left[\frac{2k_x(q)}{k_x(q) + k_x^\downarrow(q)} \right]^* \frac{k_x^\downarrow + k_x^\uparrow}{2k_x} e^{i(k_x^\downarrow x - k_x^\uparrow x)} \right|_{x \rightarrow 100}, & x > 0 \end{cases}$$

and its easy to see that $R^\sigma + T^\sigma = 1$. The transmission and reflection probability currents are conserved as expected (continuity of $\psi, \frac{\partial \psi}{\partial x}$). $\Phi = \frac{k_x^\downarrow + k_x^\uparrow}{2k_x} e^{i(k_x^\downarrow x - k_x^\uparrow x)}$. There is a discontinuity that occurs because k_x^\downarrow becomes complex for $q > 0.5K_F$. This is because wavevectors with $q > 0.5K_F$ have energy beyond the barrier, which is why the transmisson probability goes to zero for them. Also, considering $x \rightarrow 100$, changes the phase rapidly causing a steep fall in the transmitted spin current density plot in figure 4.2(c) and 4.2(d). The transverse component of the reflected spin current density has a phase associated with it, given by $\angle R_\uparrow R_\downarrow^*$ is also plotted in figure 4.2. Whereas the transverse component of the transmitted spin current density varies with the space. So, its spatial precission is shown in figure 4.3.

For further discussions, we normalize q, K_F^\uparrow and K_F^\downarrow w.r.t. K_F . Some quantities of interest were studied as a function of q for $K_F^\uparrow = 1.5K_F$ and $K_F^\downarrow = 0.5K_F$ and for both planar multilayer case and for nanowire case (Figure 4.1, 4.2 and 4.3).

4.2.1 Spin filtering

The interface slows down minority spin while speeding up majority spin. So, reflection and transmission probabilities are spin dependent (fig 4.2(a), 4.2(b), 4.2(c) and 4.2(d)). When $q > K_F^\downarrow$, the transverse spin is retained only in the reflected wave as minority spin decays in the ferromagnet (fig 4.2(e), 4.2(f)). Hence, a discontinuity occurs at $q = K_F^\downarrow$. We can define $[1 - |R_\uparrow R_\downarrow| - |T_\uparrow T_\downarrow \Phi|_{x \rightarrow \infty}]$ as a measure of transverse spin absorbed by the interface, which actually causes the spin transfer torque. In figure 4.1, the reflected and transmitted spin current densities are also plotted. The spin current densities are in terms of $\frac{\hbar}{2} v_x$ (where $v_x = \frac{k_x \hbar}{m}$).

- 1) The first plot (fig 4.2(a) and 4.2(b)) shows the variation of the reflection probability current w.r.t q .
- 2) The next plot (fig 4.2(c) and 4.2(d)) shows the variation of the transmision probability current w.r.t q .
- 3) The third plot (fig 4.2(e) and 4.2(f)) shows the variation of transverse spin current w.r.t q .

4.2.2 Spin Rotation

When $R_\uparrow R_\downarrow$ is imaginary, a phase is introduced in the reflected wave. It is quantum mechanical in nature and has no classical analogue. Figure 4.2 shows this variation of phase w.r.t. q .

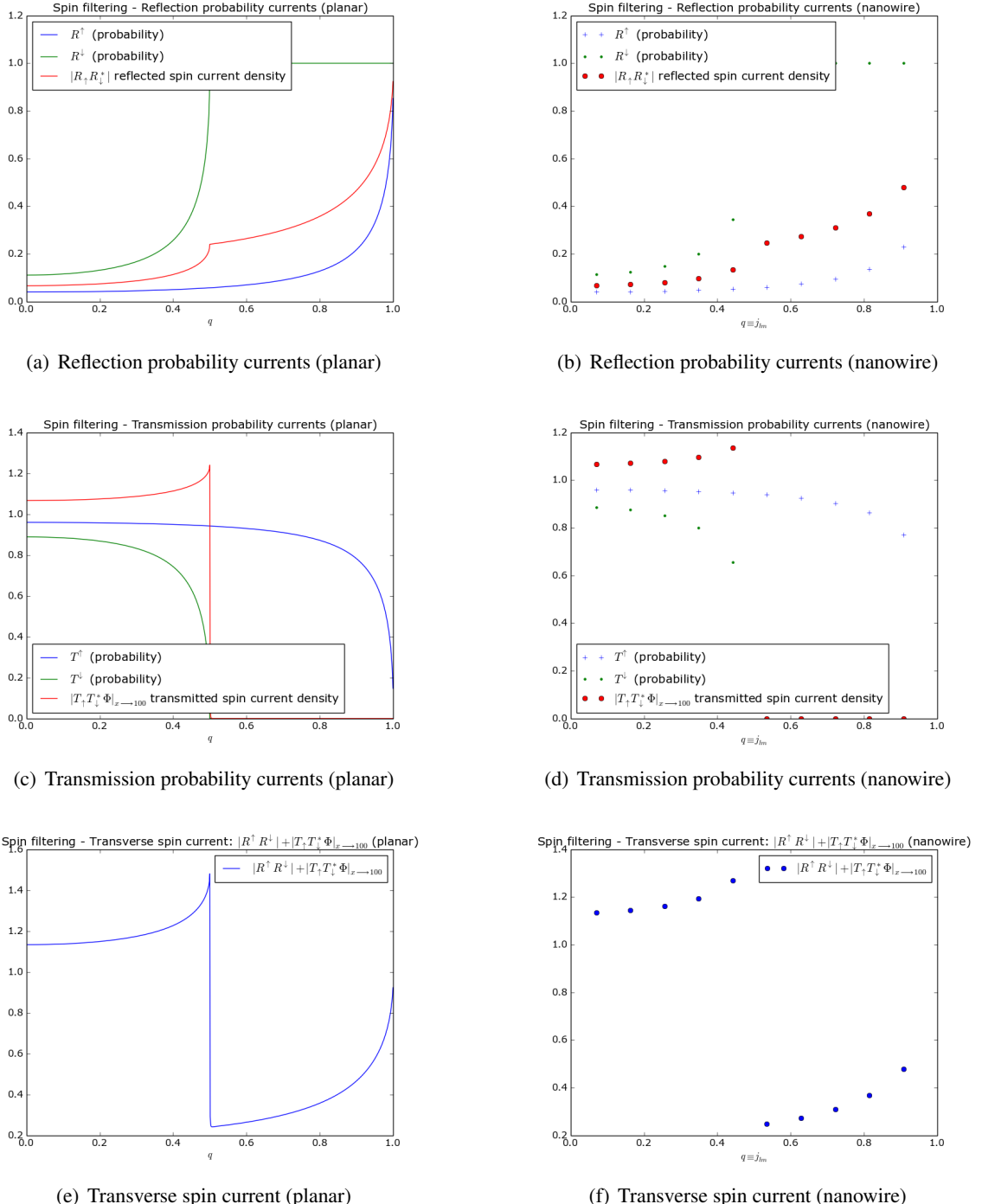


Figure 4.1: Spin filtering of spin currents for a free electron

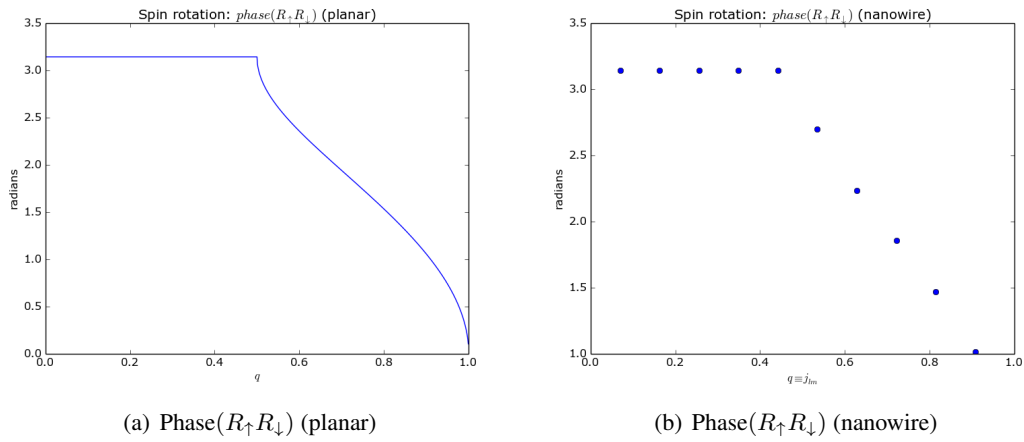


Figure 4.2: Spin rotation of spin currents for a free electron

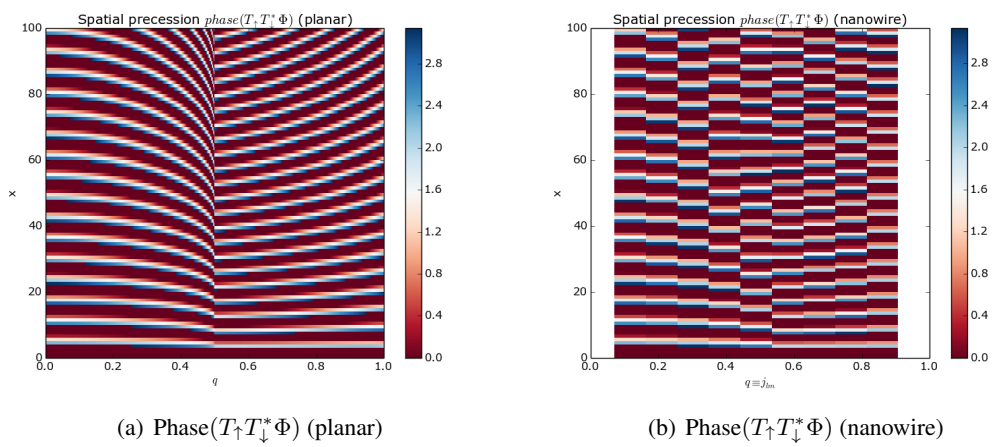


Figure 4.3: Spatial spin precession of spin currents for a free electron

4.2.3 Spatial precession

The transmitted transverse spin has a spatially varying phase (Figure 4.3) when $k_x^\uparrow \neq k_x^\downarrow$. This causes a distributed torque density at every point in the ferromagnet. One could observe that here, a constant energy level has been assumed and the probabilities of spin currents were plotted for different values of q which is nothing but the radially confined energy levels. $k_x^\sigma = \sqrt{(K_F^\sigma)^2 - q^2}$ gives us the corresponding k_x^σ either for magnetic or non-magnetic material. But if the nanowire is finitely long and becomes comparable to the radial dimensions, then this assumption would not be valid and we would have very limited energy values and mostly they might allow only very selective q and k_x^σ values.

4.3 Distribution of electrons

The spin current flowing through the non-magnetic-ferromagnetic interface were derived and plotted for a free electron case. Now, for a distribution of electrons, the spin current is given by^[39],

$$Q_{xx}^{in} = \frac{\hbar}{2} \int_{v_x > 0} \frac{d^3k}{(2\pi)^3} f_p(\mathbf{k}) v_x(\mathbf{k}) \sin \theta_{\mathbf{k}} \cos \phi_{\mathbf{k}}$$

but for a nanowire, it should be

$$Q_{xx}^{in} = \frac{\hbar}{2} \sum_{v_x > 0}^k \frac{(\Delta^3 k)}{(2\pi)^3} f_p(\mathbf{k}) v_x(\mathbf{k}) \sin \theta_{\mathbf{k}} \cos \phi_{\mathbf{k}}$$

where $f_p(\mathbf{k}) = f_\uparrow(\mathbf{k}) - f_\downarrow(\mathbf{k})$ determines the degree of the polarization at each point on the Fermi surface. The angles $\theta_{\mathbf{k}}$ and $\phi_{\mathbf{k}}$ determine the direction of the spin polarization. Electron states in the immediate vicinity of the Fermi surface dominate the transport of charge and spin. Therefore, we write

$$f_\sigma(\mathbf{k}) \rightarrow f_\sigma(\epsilon_{\mathbf{k}}) + g_\sigma(\mathbf{q}) \frac{\partial f_o(\epsilon_{\mathbf{k}})}{\partial \epsilon_k},$$

where f_o is the equilibrium Fermi-Dirac distribution function and the partial derivative restricts \mathbf{k} to the Fermi surface. We write $g_\sigma(\mathbf{q})$ rather than $g_\sigma(\mathbf{k})$ because $|\mathbf{k}|^2 = k_x^2 + q^2 = k_F^2$. The equilibrium term does not contribute to the spin current. The summation happens for different values of k_x , which in turn depends on the different values taken by \mathbf{q} . So, there are 3 summations, one over k_x and the other two over q . It is known that $E_x \propto k_x^2$ and $E_{2D} \propto q^2$.

$$Q_{xx}^{in} = \frac{\hbar}{2} \sum_{v_x > 0}^q (\Delta^2 q) \frac{1}{(2\pi)^3} g_p(\mathbf{q}) \sin \theta_{\mathbf{q}} \cos \phi_{\mathbf{q}} v_x(\mathbf{q}) \sum_{v_x > 0}^{k_x} (\Delta k_x) \frac{\partial f_o(\epsilon_{\mathbf{k}})}{\partial \epsilon_k}$$

From the Boltzmann Transport equation, we get,

$$\frac{\partial f}{\partial t} + \nabla f \cdot \frac{\mathbf{p}}{m} + \frac{\partial f}{\partial \mathbf{p}} \cdot \mathbf{F} = \frac{df}{dt} = 0$$

Ignoring bulk effects, we get at steady state,

$$\frac{\partial f}{\partial \mathbf{x}} v_x = \frac{1}{\hbar} \frac{\partial E}{\partial x} \frac{\partial f}{\partial \mathbf{k}_x}$$

which implies,

$$\frac{\partial f}{\partial E} = \frac{1}{\hbar v_x} \frac{\partial f}{\partial k_x}$$

So,

$$\sum_{v_x > 0}^{k_x} (\Delta k_x) \frac{\partial f_o(\epsilon_{\mathbf{k}})}{\partial \epsilon_k} = \sum_{v_x > 0}^{k_x} (\Delta k_x) \frac{1}{\hbar v_x} \frac{\partial f}{\partial k_x} = \frac{1}{\hbar v_x} \sum_{v_x > 0}^{k_x} \Delta f = \frac{1}{\hbar v_x}$$

(considering f as a step function). Substituting this in the equation for Q_{xx}^{in} , we get,

$$Q_{xx}^{in} = \frac{1}{4\pi} \sum_{v_x > 0}^q (\Delta^2 q) \frac{1}{(2\pi)^2} g_p(\mathbf{q}) \sin \theta_{\mathbf{q}} \cos \phi_{\mathbf{q}} \quad (4.11)$$

Similarly,

$$Q_{yx}^{in} = \frac{1}{4\pi} \sum_{v_x > 0}^q (\Delta^2 q) \frac{1}{(2\pi)^2} g_p(\mathbf{q}) \sin \theta_{\mathbf{q}} \sin \phi_{\mathbf{q}} \quad (4.12)$$

Following the similar derivation for the reflected and transmitted spin currents as mentioned in the Stiles' paper^[39], we get,

$$\begin{aligned} Q_{xx}^{ref} &= -\frac{1}{4\pi} \sum_{v_x > 0}^q (\Delta^2 q) \frac{1}{(2\pi)^2} g_p(\mathbf{q}) \sin \theta_{\mathbf{q}} |R_{\uparrow}^*(\mathbf{q}) R_{\downarrow}(\mathbf{q})| \Re \left[e^{i(\phi_q + \Delta \phi_q)} \right] \\ Q_{yx}^{ref} &= -\frac{1}{4\pi} \sum_{v_x > 0}^q (\Delta^2 q) \frac{1}{(2\pi)^2} g_p(\mathbf{q}) \sin \theta_{\mathbf{q}} |R_{\uparrow}^*(\mathbf{q}) R_{\downarrow}(\mathbf{q})| \Im \left[e^{i(\phi_q + \Delta \phi_q)} \right] \\ Q_{xx}^{tr} &= \frac{1}{4\pi} \sum_{v_x > 0}^q (\Delta^2 q) \frac{1}{(2\pi)^2} g_p(\mathbf{q}) \sin \theta_{\mathbf{q}} \frac{v_x^{\uparrow}(\mathbf{q}) + v_x^{\downarrow}(\mathbf{q})}{|2v_x(\mathbf{q})|} \Re \left[T_{\uparrow}^*(\mathbf{q}) T_{\downarrow}(\mathbf{q}) e^{i\phi_q} e^{-i(k_x^{\uparrow} - k_x^{\downarrow})x} \right] \\ Q_{yx}^{tr} &= \frac{1}{4\pi} \sum_{v_x > 0}^q (\Delta^2 q) \frac{1}{(2\pi)^2} g_p(\mathbf{q}) \sin \theta_{\mathbf{q}} \frac{v_x^{\uparrow}(\mathbf{q}) + v_x^{\downarrow}(\mathbf{q})}{|2v_x(\mathbf{q})|} \Im \left[T_{\uparrow}^*(\mathbf{q}) T_{\downarrow}(\mathbf{q}) e^{i\phi_q} e^{-i(k_x^{\uparrow} - k_x^{\downarrow})x} \right] \end{aligned}$$

At this point, we must make a specific choice for $g_p(\mathbf{q})$ and the polarization of the incident spin current. Let us assume the current is completely spin polarized along $+\hat{\mathbf{x}}$. This fixes $\theta_{\mathbf{k}} = \pi/2$ and $\phi_{\mathbf{k}} = 0$. Then, from (4.12), $Q_{yx}^{in} = 0$ and Q_{xx}^{in} is the only incoming transverse component. We begin with the approximate form, $g_p(\mathbf{q}) = a + b v_x(\mathbf{q})$. The two terms account for interface and bulk effects, respectively. The velocity-dependent bulk term is familiar from textbook treatments of electrical conductivity^[40], usually gradients in spin accumulation rather than electric potential drive the spin current in the nonmagnet. The constant term is needed because a spin-dependent chemical potential difference $\Delta\mu$ across an interface also drives a spin current^[41]. Here, we assume that the interface resistance is large (i.e. large

reflection probability), so we use $g_p(\mathbf{q}) \simeq a = \Delta\mu$. With these choices, the incident spin current is

$$Q_{xx}^{in} = \frac{1}{4\pi} \frac{\Delta\mu}{(2\pi)^2} \sum_{v_x > 0}^q (\Delta^2 q)$$

The summation depends on the nanowire symmetry that we use. Similarly, the other components for $\theta_{\mathbf{q}} = \pi/2$ and $\phi_{\mathbf{q}} = 0$ are:

$$Q_{xx}^{ref} = -\frac{1}{4\pi} \frac{\Delta\mu}{(2\pi)^2} \sum_{v_x > 0}^q (\Delta^2 q) |R_{\uparrow}^*(\mathbf{q}) R_{\downarrow}(\mathbf{q})| \Re [e^{i\Delta\phi_q}] \quad (4.13)$$

$$Q_{yx}^{ref} = -\frac{1}{4\pi} \frac{\Delta\mu}{(2\pi)^2} \sum_{v_x > 0}^q (\Delta^2 q) |R_{\uparrow}^*(\mathbf{q}) R_{\downarrow}(\mathbf{q})| \Im [e^{i\Delta\phi_q}] \quad (4.14)$$

$$Q_{xx}^{tr} = \frac{1}{4\pi} \frac{\Delta\mu}{(2\pi)^2} \sum_{v_x > 0}^q (\Delta^2 q) \frac{v_x^{\uparrow}(\mathbf{q}) + v_x^{\downarrow}(\mathbf{q})}{|2v_x(\mathbf{q})|} \Re \left[T_{\uparrow}^*(\mathbf{q}) T_{\downarrow}(\mathbf{q}) e^{-i(k_x^{\uparrow} - k_x^{\downarrow})x} \right] \quad (4.15)$$

$$Q_{yx}^{tr} = \frac{1}{4\pi} \frac{\Delta\mu}{(2\pi)^2} \sum_{v_x > 0}^q (\Delta^2 q) \frac{v_x^{\uparrow}(\mathbf{q}) + v_x^{\downarrow}(\mathbf{q})}{|2v_x(\mathbf{q})|} \Im \left[T_{\uparrow}^*(\mathbf{q}) T_{\downarrow}(\mathbf{q}) e^{-i(k_x^{\uparrow} - k_x^{\downarrow})x} \right] \quad (4.16)$$

From the above equations, the magnitude of the reflected (from eqns. (4.13) and (4.14)) and transmitted (from eqns. (4.15) and (4.16)) transverse spin current could be determined relative to the incoming transverse component of spin current Q_{xx}^{in} ,

$$\frac{|Q_{xx}^{ref} + Q_{yx}^{ref}|}{Q_{xx}^{in}} = \frac{\sum_{k_x > 0}^q (\Delta^2 q) |R_{\uparrow}^*(\mathbf{q}) R_{\downarrow}(\mathbf{q})|}{\sum_{k_x > 0}^q (\Delta^2 q)} \quad (4.17)$$

$$\frac{|Q_{xx}^{tr} + Q_{yx}^{tr}|}{Q_{xx}^{in}} = \frac{\sum_{k_x > 0}^q (\Delta^2 q) \left| \frac{k_x^{\uparrow}(\mathbf{q}) + k_x^{\downarrow}(\mathbf{q})}{2k_x(\mathbf{q})} T_{\uparrow}^*(\mathbf{q}) T_{\downarrow}(\mathbf{q}) e^{-i(k_x^{\uparrow} - k_x^{\downarrow})x} \right|}{\sum_{k_x > 0}^q (\Delta^2 q)} \quad (4.18)$$

Now, using the relations in (4.10) the above summations were calculated for different geometries to understand how confining electrons in a low-dimensional structures change the spin-transfer torque experienced by the ferromagnetic layer.

4.3.1 Transverse spin current for different wire sizes

Using the relation obtained in (4.17), the reflected transverse spin current is plotted for nanowire structures with different sizes⁵(fig 4.4)

Bigger the size of the wire, more number of states are allowed and hence more spin current. The fraction of the electrons that gets reflected from the interface compared to the ones that are incident, is almost a constant, so it increases slowly. Next, the transverse transmitted spin current is plotted in fig 4.5.

⁵ l_w is same as L_x and L_y . $l_w = L_x = L_y \rightarrow$ length of one side of the cross-section of the wire.

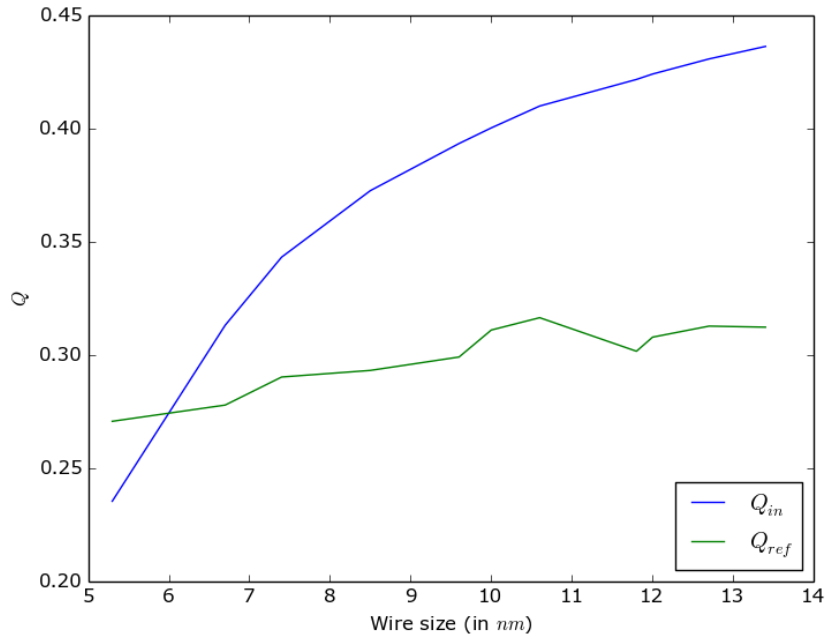


Figure 4.4: Incident and reflected transverse spin current density vs l_w in nm

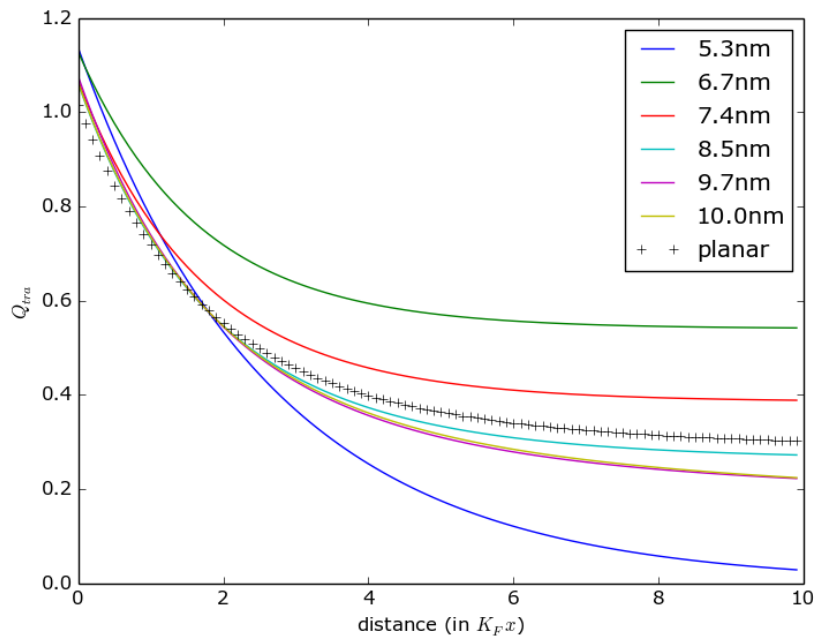


Figure 4.5: $Q_{transmitted}^{(transverse)}$ vs $K_F x$ for different wires

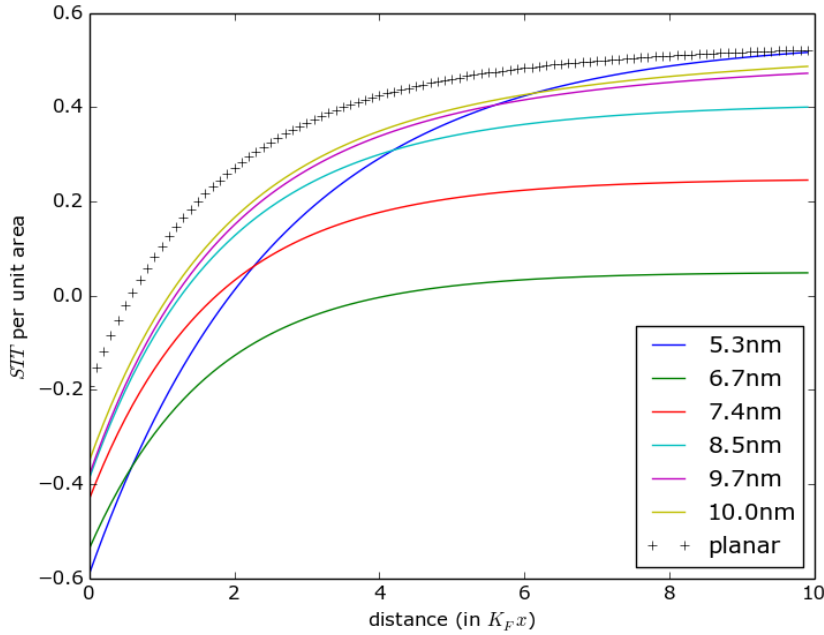


Figure 4.6: Spin Transfer Torque vs $K_F x$ for different wires

As expected, it falls down as it goes through the wires of any dimensions. This is due to spatial precession. When the size increases, the number of electrons that cross the barrier increases and also the number of electrons that tunnel through also increases. The combined effect of both of them results in damped oscillation w.r.t $K_F x$ or just damping. It depends on the size, difference in K_F^\downarrow and K_F^\uparrow , etc.

4.3.2 Spin Transfer Torque for different wire sizes

The spin-transfer torque^[39] is given by, $N_{stt} = (\mathbf{Q}_{in} - \mathbf{Q}_{tr} + \mathbf{Q}_{ref}) \cdot A\hat{x}$. Here, N_{stt} is higher for larger wires (except for $l_w = 5.3\text{nm}$ case) (from fig (4.6)), because reflection or scattering supports in increasing the torque. There are more of the electrons too to further it.

Just to get more insight, the same figure 4.6 is shown from the other side in fig 4.7, i.e. here the behaviour of the same N_{stt} is shown as the size of the wire changes, sampled at different distances ($K_F x = 0, K_F x = 2.5, K_F x = 5, K_F x = 7.5$ and $K_F x = 10$)

There is an overall apparent increase in N_{stt} as the wire size increases, but some glitches happen because the balance mentioned earlier varies a lot when there are very few allowed energy levels (like the case of wire with size $l_w = 6.7\text{nm}$, which has only 4 allowed energy levels).

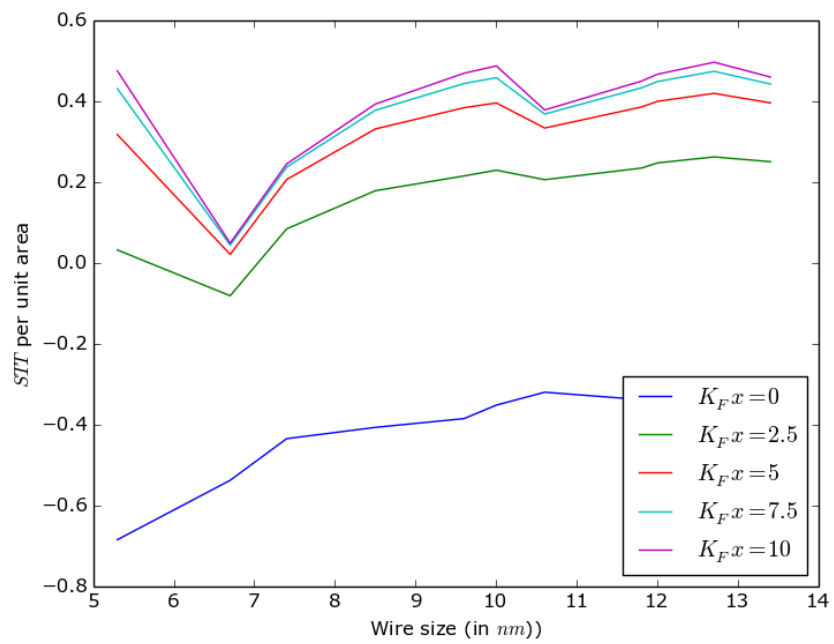


Figure 4.7: Spin Transfer Torque vs l_w at $K_F x = 10$

CHAPTER 5

Conclusion and future scope for work

The behaviour of TMR for different wire sizes and barrier potentials could also be studied for different outside potentials (i.e. lattice potentials). The variation of STT in nanowire structures have to be studied for materials with lattice-matched interfaces.

It is interesting to note that, there is a growing interest in the resistance and magnetoresistance associated with domain walls (DWs) in metallic ferromagnets^[42]. Owing to recent progress in nanotechnology, it became possible now to extract a single DW contribution to electrical resistance^{[42]–[45]}. Surprisingly, it turned out that the resistance of a system with DWs in some cases was smaller than in the absence of DWs^{[43],[44]}, whereas in other cases it was larger^{[46]–[48]}. This intriguing observation led to considerable theoretical interest in electronic transport through DWs. The interest is additionally stimulated by possible applications of the associated magnetoresistance in magnetoelectronics devices.

In a series of experiments the magnetoresistance associated with DWs was found to be very large. Moreover, recent experiments on Ni microjunctions showed that constrained DWs at the contact between ferromagnetic wires produce an unexpectedly large contribution to electrical resistivity, and consequently lead to a huge negative magnetoresistance. It was shown theoretically that DWs in magnetic microjunctions can be very sharp, with the characteristic width L being of atomic scale. This is much less than typical DW width in bulk materials or thin films^[49].

The variation of resistances and spin transfer torques of the domain wall^[50] while taking into account of its motion, have to be studied for various dimensions of nanowire (or nanopillar)^[51].

REFERENCES

- [1] Harrison P., "Quantum Wells, Wires and Dots", Wiley, New York, 2001
- [2] Datta S., "Electronic Transport in Mesoscopic Systems," Cambridge University Press, 15-May-1997
- [3] Wissner Gross A. D., "Dielectrophoretic reconfiguration of nanowire interconnects," Nanotechnology 17: 4986-4990, 2006
- [4] Grange R., Choi J.W., Hsieh C.L., Pu Y., Magrez A., Smajda R., Forro L., Psaltis D., "Lithium niobate nanowires: synthesis, optical properties and manipulation". Applied Physics Letters 95: 143105, 2009
- [5] Vizcaino J. L. P., Nunez C. G. A., "Fast, effective manipulation of nanowires for electronic devices". SPIE Newsroom, 2013
- [6] Sakurai J. J., "Modern Quantum Mechanics," Pearson Education Inc., 1994
- [7] Hindmarsh A. C., "ODEPACK, A Systematized Collection of ODE Solvers," in Scientific Computing, R. S. Stepleman et al. (eds.), North-Holland, Amsterdam, (vol. 1 of IMACS Transactions on Scientific Computation), pp. 55-64, 1983
- [8] Radhakrishnan K., Hindmarsh A. C., "Description and Use of LSODE, the Livermore Solver for Ordinary Differential Equations," Lawrence Livermore National Laboratory Report UCRL-ID-113855, NASA Reference Publication 1327, 1993
- [9] Hairer E., NÅrsett S. P., Wanner G., "Solving ordinary differential equations I: Nonstiff problems (2nd ed.)", Berlin: Springer Verlag, ISBN 978-3-540-56670-0, 1993
- [10] Butcher J. C., "Numerical Methods for Ordinary Differential Equations", John Wiley, ISBN 978-0-471-96758-3, 2003
- [11] Quarteroni A., Sacco R., Saleri F., "Matematica Numerica", Springer Verlag, ISBN 978-88-470-0077-3, 2000
- [12] Iserles A., "A First Course in the Numerical Analysis of Differential Equations", Cambridge University Press, ISBN 978-0-521-55655-2, 1996
- [13] Eisenhart L. P., "Enumeration of Potentials for Which One-Particle Schroedinger Equations are Separable", Physical Review, Volume 74, Number 1, July 1, 1948.
- [14] Vanek P., Mandel J. and Brezina M., Denver, "Algebraic Multigrid by Smoothed Aggregation for Second and Fourth Order Elliptic Problems.", Computing 56, 179-196, 1996
- [15] Knyazev A. V., "Toward the optimal preconditioned eigen solver: Locally Optimal Block Preconditioned Conjugate Gradient method.", SIAM J. SCI. COMPUT. Vol. 23, No. 2, pp. 517-541, 2001
- [16] Knyazev A. V., Argentati M. E., Lashuk I., and Ovtchinnikov E. E., "Block Locally Optimal Preconditioned Eigenvalue Xolvers (BLOPEX) in HYPRE and PETSC," 2007
- [17] Imamura H. and Maekawa S., "Theory of Spin-Dependent Tunneling" from Part 7 of "Handbook of Magnetism and Advanced Magnetic Materials". Volume 1: Fundamentals and Theory. 2007 John Wiley & Sons, Ltd. ISBN: 978-0-470-02217-7
- [18] J. S. Moodera, L. R. Kinder, T. M. Wong, and R. Meservey, Phys. Rev. Lett. 74, 3273 1995
- [19] T. Miyazaki and N. Tezuka, J. Magn. Magn. Mater. 139, L231 1995
- [20] M. Julliere, Phys. Lett. 54A, 225 1975

- [21] S. Maekawa and U. Gavert, IEEE Trans. Magn. MAG-18, 707 1982
- [22] R. Meservey and P. M. Tedrow, Phys. Rep. 238, 173 1994
- [23] J. Inoue and S. Maekawa, Phys. Rev. B 53, R11 927 1996
- [24] J. Bardeen, Phys. Rev. Lett. 6, 57 1961
- [25] J. C. Slonczewski, Phys. Rev. B 39, 6995 1989
- [26] J. Mathon, Phys. Rev. B 56, 11 810 1997
- [27] Burstein, E. and Lundqvist, S. (Eds.) (1969). Tunneling Phenomena in Solids, Plenum Press: New York
- [28] Zhang, S. and Levy, P. (1999). Models for magnetoresistance in tunnel junctions. European Physical Journal B, 10, 599
- [29] J.C. Slonczewski, J. Magn. Magn. Mater. 159, L1 1996; 195, L261 1999.
- [30] L. Berger, Phys. Rev. B 54, 9353 1996; J. Appl. Phys. 81, 4880 1997; Phys. Rev. B 59, 11 465 1999; J. Appl. Phys. 89, 5521 2001; J. Appl. Phys. 91, 6795 2002
- [31] M. Tsoi, A.G.M. Jansen, J. Bass, W.C. Chiang, M. Seck, V. Tsoi, P. Wyder, Phys. Rev. Lett. 80, 4281 1998; J.Z. Sun, J. Magn. Magn. Mater. 202, 157 1999; J.-E. Wegrowe, D. Kelly, Ph. Guittienne, Y. Jaccard, and J.Ph. Ansermet, Europhys. Lett. 45, 626 1999
- [32] A. Fert and P. Bruno, in Ultrathin Magnetic Structure II, edited by B. Heinrich and J.A.C. Bland Springer-Verlag, Berlin, 1994
- [33] E.B. Myers, D.C. Ralph, J.A. Katine, R.N. Louie, and R.A. Buhrman, Science 285, 867 1999; J.A. Katine, F.J. Albert, R.A. Buhrman, E.B. Myers, and D.C. Ralph, Phys. Rev. Lett. 84, 3149 2000
- [34] J. Grollier, V. Cros, A. Hamzic, J.M. George, H. Jaffre s, A. Fert, G. Faini, J. Ben Youssef, and H. Legall, Appl. Phys. Lett. 78, 3663 2001
- [35] J.-E. Wegrowe, D. Kelly, T. Truong, Ph. Guittienne, and J.-Ph. Ansermet, Europhys. Lett. 56, 748 2001
- [36] W. Weber, S. Riesen, and H.C. Siegmann, Science 291, 1015 2001
- [37] R. Urban, G. Woltersdorf, and B. Heinrich, Phys. Rev. Lett. 87, 217 204 2001
- [38] G.A. Prinz, J. Magn. Magn. Mater. 200, 57 1999
- [39] M. D. Stiles and A. Zangwill, Phys. Rev. B 66, 014407 2002
- [40] J. M. Ziman, Principles of the Theory of Solids Cambridge University Press, Cambridge, England, 1972, Chap. 7
- [41] A.G. Aronov, JETP Lett. 24, 32 1977; M. Johnson and R.H. Silsbee, Phys. Rev. B 35, 4959 1987; P.C. van Son, H. van Kempen, and P. Wyder, Phys. Rev. Lett. 58, 2271 1987
- [42] A.D. Kent, J. Yu, U. Ru diger, and S.S.P. Parkin, J. Phys.: Condens. Matter 13, R461 2001
- [43] K. Hong and N. Giordano, J. Phys.: Condens. Matter 13, L401 1998
- [44] U. Ruediger, J. Yu, S. Zhang, A.D. Kent, and S.S.P. Parkin, Phys. Rev. Lett. 80, 5639 1998
- [45] A.D. Kent, U. Ru diger, J. Yu, L. Thomas, and S.S.P. Parkin, J. Appl. Phys. 85, 5243 1999
- [46] J.F. Gregg, W. Allen, K. Ounadjela, M. Viret, M. Hehn, S.M. Thompson, and J.M.D. Coey, Phys. Rev. Lett. 77, 1580 1996
- [47] N. Garcia, M. Munoz, and Y.-W. Zhao, Phys. Rev. Lett. 82, 2923 1999
- [48] U. Ebels, A. Radulescu, Y. Henry, L. Piraux, and K. Ounadjela, Phys. Rev. Lett. 84, 983 2000.

- [49] V. K. Dugaev, J. Berakdar, and J. Barnas, Phys. Rev. B 68, 104434 2003
- [50] V. K. Dugaev, V. R. Vieira, P. D. Sacramento, J. Barnas, M. A. N. Araujo, and J. Berakdar, Phys. Rev. B 74, 054403 2006
- [51] Articles by Andre Thiaville, Yoshinobu Nakatani and Mark D. Stiles, Jacques Miltat in "Spin Dynamics in Confined Magnetic Structures III," edited by Hillebrands B., Thiaville A. Springer, Berlin, 2006, pp. 161-206, & pp. 225-308